Silicon nanowire heterostructures for advanced energy and environmental applications: A review

Article *in* Nanotechnology · November 2016

DOI: 10.1088/0957-4484/28/1/012001

2 authors:

Ramesh Ghosh
Seoul National University
18 PUBLICATIONS **60** CITATIONS

SEE PROFILE

Pravat K Giri
Indian Institute of Technology Guwahati
174 PUBLICATIONS **1,749** CITATIONS

SEE PROFILE

Silicon nanowire heterostructures for advanced energy and environmental applications: a review

2017 Nanotechnology 28 012001

(http://iopscience.iop.org/0957-4484/28/1/012001)

IOP Publishing Nanotechnology
Nanotechnology 28 (2017) 012001 (26pp) doi:10.1088/0957-4484/28/1/012001

Topical Review

Silicon nanowire heterostructures for advanced energy and environmental applications: a review

Ramesh Ghosh[1] **and P K Giri**[1,2]

[1] Department of Physics, Indian Institute of Technology Guwahati, Guwahati 781039, India
[2] Centre for Nanotechnology, Indian Institute of Technology Guwahati, Guwahati 781039, India

E-mail: giri@iitg.ernet.in

Received 27 June 2016, revised 29 September 2016
Accepted for publication 6 October 2016
Published 28 November 2016

Abstract

Semiconductor nanowires (NWs), in particular Si NWs, have attracted much attention in the last decade for their unique electronic properties and potential applications in several emerging areas. With the introduction of heterostructures (HSs) on NWs, new functionalities are obtained and the device performance is improved significantly in many cases. Due to the easy fabrication techniques, excellent optoelectronic properties and compatibility of forming HSs with different inorganic/organic materials, Si NW HSs have been utilized in various configurations and device architectures. Herein, we review the recent developments in Si NW HS-based devices including the fabrication techniques, properties (e.g., light emitting, antireflective, photocatalytic, electrical, photovoltaic, sensing etc) and related emerging applications in energy generation, conversion, storage, and environmental cleaning and monitoring. In particular, recent advances in Si NW HS-based solar photovoltaics, light-emitting devices, thermoelectrics, Li-ion batteries, supercapacitors, hydrogen generation, artificial photosynthesis, photocatalytic degradation of organic dyes in water treatment, chemical and gas sensors, biomolecular sensors for microbial monitoring etc have been addressed in detail. The problems and challenges in utilizing Si NW HSs in device applications and the key parameters to improve the device performance are pointed out. The recent trends in the commercial applications of Si NW HS-based devices and future outlook of the field are presented at the end.

Keywords: nanowire heterostructures, energy applications, environmental applications, review

(Some figures may appear in colour only in the online journal)

1. Introduction

The energy and environment are two of the biggest challenges of the 21st century to meet the world's growing energy demand, particularly pertaining to the industrialization and fast growing market for portable electronic devices. The crisis of conventional fossil fuels and the ever growing environmental pollution due to widespread industrialization have left a strong impact on the environment and this has inspired worldwide attention to search for alternative energy sources, advanced energy conversion and storage technologies. The sun, the source of unlimited energy, is considered as the ultimate alternative to meet our future energy demands and environmental sustainability. In this regard, photovoltaics and photocatalysed water splitting have emerged as two promising ways towards efficient utilization of solar energy. In addition, the development of advanced energy storage devices is considered equally significant in proper utilization of energy. However, there are several issues to address in the energy and environmental challenges, such as (a) optimization of power consumption, (b) energy utilization efficiency, (c) device stability, (d) flexibility, (e) device

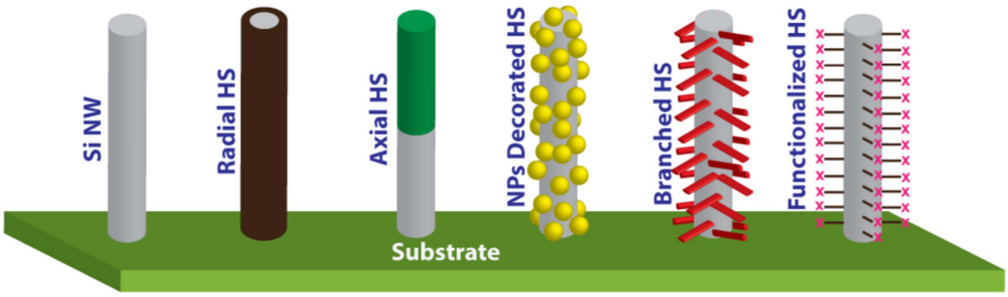

Figure 1. Schematic illustration of the commonly studied HSs based on Si NWs.

performance, (f) cost reduction etc. The design and creation of new materials and substances chemically modified at the molecular and atomic levels promise new technology that may be able to overcome some of the key issues for the energy and environmental challenges.

During the past decades, one-dimensional (1D) semiconductor nanostructures, including nanowires (NWs), nanorods (NRs), nanotubes, nanofibers (NFs) and nanobelts, have been attracting a great deal of attention in both basic scientific research and potential technological applications due to their fascinating physical and chemical characteristics [1–17]. In the important class of semiconductors, Si nanostructures, especially Si NWs, are extensively studied due to their ease of synthesis, fascinating properties and application in a wide range of areas, such as field-effect transistors (FETs), light-emitting diodes (LEDs), solar cells, Li-ion batteries, photochemical reactors, chemical and biosensors, photodetectors etc [1–17]. Over the past decades, various types of 1D Si nanostructure have been fabricated by several groups worldwide using various methods, such as chemical vapor deposition (CVD), pulsed laser deposition (PLD), thermal evaporation, template-assisted growth, molecular beam epitaxy (MBE), reactive ion etching (RIE), metal-assisted chemical etching (MACE) etc [4, 13, 18–27]. A number of excellent reviews and reports on the preparation, modification, assembly, characterization, properties, engineering and applications of Si NWs have been published [1–14, 28]. However, the key parameters of the performance index of the bare Si NW-based nanodevices often do not meet the level demanded for practical applications. Therefore, together with effective synthesis strategies, significant improvements are required in the design and fabrication of Si NWs to meet future demands for applications in a variety of fields. The modification of the surface of the Si NWs by using hybrid structures or a heterostructure (HS) approach could enable superior/efficient performance of the nanoscale devices. In the past few years, several methodologies have been developed for the fabrication of high-quality Si NW HSs with suitable external materials. Many of the recent reports on semiconductor NW HSs in general highlight the significant advantages of the HS approach. In the HS approach, by incorporating novel materials with additional functionalities and complexities, researchers are able to modify/improve the selective properties of the NWs according to the requirements. In particular, many works have been devoted to the fabrication of HSs based on compound semiconductors (e.g., group II–VI, III–V etc), that find widespread applications in optoelectronics, photonics, sensors etc. On the other hand, fewer reports are available on group IV semiconductor NW HSs. The HS devices often exhibit efficient and improved performance in comparison to the bare NW counterpart.

In this review, we first present a summary of the widely used techniques for the growth of high-quality Si NWs and methodologies for the fabrication of various types of HS on Si NWs, such as core–shell radial HSs, axial HSs, hierarchical HSs, quantum dot (QD)-decorated NW HSs and functionalized NW HSs. Next, we focus on the recent advances in the use of Si NW-based HSs for advanced energy and environmental applications, such as LEDs, solar photovoltaics, Li-ion batteries, photocatalytic degradation of dyes and water purification, chemical and gas sensors etc. The problems and challenges of utilizing Si NW HSs in various devices and the key parameters to improve the device performance are extensively discussed to highlight the effectiveness of the HS approach. The recent developments in the commercialization of the Si NW HSs and future directions for further improvement in this field are presented at the end.

2. Fabrication of Si nanowire heterostructures

After the award of the Physics Nobel Prize in 2000 for the discovery of 'The double heterostructure: concept and its application in physics, electronics and technology', HSs of different materials are being intensely investigated to exploit the functional properties arising from junctions of different materials [29]. Since HSs provide additional functionality and tunability, the properties of Si NWs can be tuned by incorporating suitable external materials according to the requirements. Several reports have been published on Si NW-based HSs, and both organic/inorganic materials as well as different combinations of them are used as the HS materials [30–83]. In this article, five different classes of NW HSs are discussed: (a) core–shell radial HSs, (b) axial HSs, (c) NPs decorated HSs, (d) branched/hierarchical HSs and (e) functionalized HSs [30–86]. Figure 1 shows a schematic of different kinds of Si NW HS. Herein, we revisited the use of various strategies for the fabrication of different types of Si NW and their HSs. In most of the cases, *ex situ* processes have been used for the fabrication of the Si NW HSs.

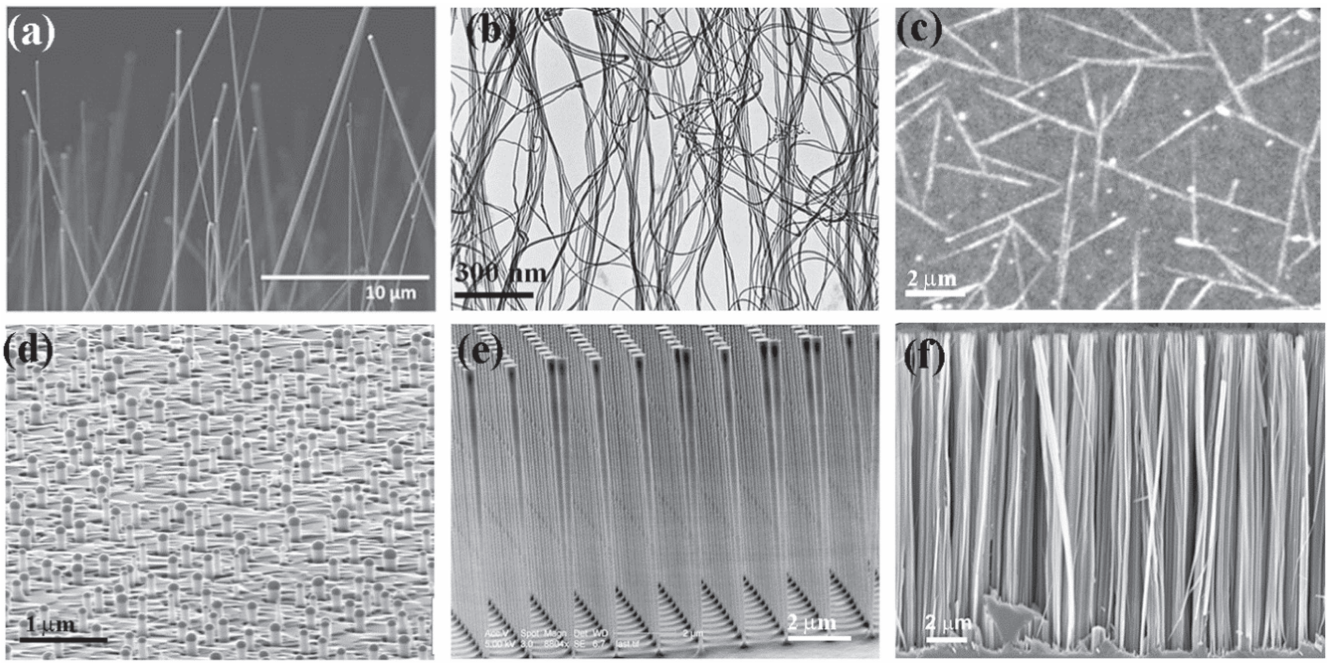

Figure 2. Si NWs grown by different processes: (a) CVD [87], copyright 2013 Royal Society of Chemistry, (b) PLD [88], copyright 1998 AIP Publishing LLC, (c) sputtering [89], copyright 2002 World Scientific Publishing Co., Inc., (d) MBE [18], copyright 2004 AIP Publishing LLC, (e) RIE [90], copyright 2009 AIP Publishing LLC, and (f) MACE [22], copyright 2014 IOP Publishing.

2.1. Synthesis of Si nanowires

The method of fabrication of Si NWs has a strong influence on their properties. The production of a large-area, highly oriented array of crystalline Si NWs with tunable properties is extremely important for achieving high-performance devices. Over the past decade, concerted efforts have been made towards the fabrication of Si NWs according to the requirements for dedicated applications. The reported methods for the fabrication of Si NWs are classified into two main approaches: bottom up and top down. The bottom-up approach, which is one of the oldest methods for the fabrication of Si NWs, is a process of gathering Si atoms in a sequence to form Si NWs. Among several bottom-up approaches, CVD via a vapor–liquid–solid (VLS) process, MBE, PLD and thermal evaporation are commonly used. Figure 2 shows FESEM images of Si NWs grown by a variety of fabrication techniques. The top-down approach is the selective reduction of bulk Si wafer by RIE and MACE to form an array of Si NWs. Of the traditional approaches, CVD and MACE methods are the most widely used for their versatility with controllability, repeatability, quality, relatively lower cost and mass production. Several review articles have addressed the synthesis of Si NWs [1–14]. Among the bottom-up fabrication methods, the CVD approach offers the concrete capability of fabricating Si NWs with controlled diameter, density, length, position and doping characteristics, suitable for device applications [12, 15, 21, 27]. CVD growth of Si NWs requires a suitable noble metal (Au, Al, Cu, Fe etc), which serves as a catalyst, and a gaseous Si precursor, such as silane (SiH_4), Si tetrachloride ($SiCl_4$) etc, which is often difficult to handle. The metal catalysts remain unaltered during the NW growth and the presence of metallic contaminations may adversely affect the intrinsic properties of the Si NWs and eventually may deteriorate the device performance. However, the CVD-grown Si NWs are desirable for complementary metal oxide semiconductor (CMOS) applications due to their process compatibility [8, 15]. PLD is another successful method for the controlled fabrication of Si NWs. However, the need for a high-energy, focused pulsed laser involving high cost of ownership prevents this method from having wide usage [10, 20, 88]. Thermal evaporation is a relatively simple fabrication technique to produce large-area, high-purity and ultralong Si NWs [12, 25, 91–93]. SiO powder is often used as the Si precursor and this process is often referred as oxide-assisted growth. However, it is difficult to control the orientation of the NWs by this method and it also results in a thick SiO_2 layer on the Si NWs. MBE is a relatively sophisticated method for the growth of high-quality Si NWs [18, 94–96]. The growth mechanism of Si NWs in the MBE process is very similar to a typical CVD process. However, due to the requirement of ultrahigh vacuum and a slow growth rate as compared to the other bottom-up approaches, MBE is less commonly used for Si NW growth. In contrast to bottom-up approaches, top-down processes are more commonly adopted for the fabrication of ordered arrays of Si NWs of controlled size, density, and tunable properties.

Among the various top-down approaches, RIE has been extensively used for the fabrication of ordered array of Si NWs, and these have been successfully exploited is large-scale fabrication of high-performance NW-based devices. This is generally an anisotropic process involving the dry etching of Si or SiO_2 by halogen radicals to grow a vertical array of Si NWs of varying aspect ratio [4, 13, 19, 90, 97, 98]. The fluorine radicals from the plasma reach the Si surface and

form volatile SiF_x, and therefore impede the side wall etching [19, 97, 98]. Anisotropic RIE with a mixture of SF_6 and O_2 gas was studied in detail by Jansen *et al* for the growth of Si NWs [97]. On the other hand, the solution-based MACE process has recently emerged as a promising and a significant tool for the rapid production of large-area, aligned and well controlled Si NWs, and it has become the most common method for the production of high-quality Si NWs [7, 9, 22–24, 99–103]. MACE requires a galvanic displacement of noble metal NPs as a catalyst on the surface of the crystalline Si substrate. However, the shape and size, length, diameter, density, crystallinity and properties of the Si NWs strongly depend on several factors, such as (a) the nature of the noble metal, (b) the shape and size of the noble metal and the intermediate distance between them, (c) the etching solution and its concentration, (d) the doping type, resistivity and the orientation of the starting Si wafer, (e) the etching temperature, (f) the etching duration etc [7, 9, 22–24, 26, 99, 101, 103–105]. Note that both RIE and MACE processes without a protective layer or masking are anisotropic and the nanostructures formed are highly nonuniform. In the literature, self-assembling polymers and lithography are generally used for patterning the noble metal on the Si wafer to control the diameter of the Si NWs and the spacing between them [43, 101–103, 105, 106]. Careful investigations have revealed that the MACE-grown Si NWs often have a rough surface due to the side wall etching, and this results in arbitrary-shaped Si NCs on the NW surface, which strongly influence its optoelectronic properties [7, 22, 100, 103, 107]. Several interesting review articles have appeared recently on the controlled synthesis, novel properties and device applications of MACE-grown Si NWs [2–9, 104, 108]. Easy fabrication process, compatibility to create HSs with other organic and inorganic materials and significant device performance are the major advantages of the MACE process for the growth of large-area, ordered and uniform Si NWs. However, the reproducibility of the process is one of the major concerns for the practical applications of MACE-grown Si NWs.

2.2. Core–shell nanowire heterostructures

The simplest and maybe the most fundamental form of NW HSs is the coaxial core–shell radial HSs. Core–shell HSs are generally formed by *ex situ* deposition of materials (shell) on the already grown NWs (core). Formation of core–multishell HSs by sequential modulation of the composition along the radial direction enables the passivation of interface states and thereby improves the overall performance of the semiconductor devices using such HSs. In this section, we discuss the fabrication of Si NW-based core–shell HSs considering the Si NWs as the core and different inorganic/organic semiconductors and metals as the shell materials. Several studies have been devoted to the effects of coating of thin layers (1–30 Å) of inorganic materials such as SiO_x [20, 109], ZnO [75–78, 86], Al_2O_3 [110], TiO_2 [72, 79–81], Fe_2O_3 [82], SiN_x [111], CdS [68, 112, 113], CdSe [83], SiC [114], ZnS [65], InP [113], SnO_2, Ge [66, 67, 115], etc and organic materials such as PDEF [71], P3HT [70], PEDOT:PSS [69, 85], TAPC [69], TMAH [84], different forms of carbon [39, 87, 116–121] (graphene, graphite, reduced graphene oxide (RGO), carbon nanotubes (CNTs) etc) on Si NWs. Si NW core–multishell HSs with different materials such as SnO_2/Fe_2O_3 [122], Al_2O_3/TiO_2 [123], Ge/Si [67], ZnS/AZO [65], CdS/AZO [68], CdS/CdSe [124], ZnO/TiO_2 [51], Ti/TiN [125] and a-Si/Al_2O_3 [126] have also been developed for improvement of the device performance. ZnO is one of the widely used semiconductors to form Si NW/ZnO core–shell HSs for photodiode, LED and photovoltaic applications [74–77, 86]. ZnO has been deposited on Si NWs by different techniques, e.g., atomic layer deposition (ALD), CVD, solution synthesis, and RF magnetron sputtering, to fabricate Si NW/ZnO device prototypes [73–78]. Ghosh *et al* reported Si NW/ZnO film core–shell HSs formed by sputtering of ZnO film on MACE-grown Si NWs and studied their photoluminescence spectral evolution [74, 108]. Figures 3(a) and (b) show the FESEM top-view and cross-sectional-view images of the Si NW/ZnO core–shell HS, respectively [74]. Sun *et al* fabricated Si NW/ZnO core–shell HSs by coating ZnO using the MOCVD method [73]. A 20 nm Al_2O_3 film was deposited by ALD on Si nanopillars grown by the RIE to form a highly efficient (22.1%) core–shell HS solar cell [110]. The Si NW/hematite (α-Fe_2O_3) core–shell HS system was studied by Mayer *et al* for photoelectrochemical (PEC) water splitting at low applied potentials [82]. Note that the Si NWs are very reactive in air ambient and this results in a native SiO_x ($0 \leqslant x \leqslant 2$) layer on the surface of the Si NWs [20, 22, 74, 99, 107–109]. The SiO_x layer on the Si NWs often plays a crucial role to modify the optoelectronic and mechanical properties of the Si NWs due to the presence of different kinds of defect in the Si–SiO_x interface. In some cases, the SiO_x layer was intentionally grown on Si NWs to form Si NW/SiO_x HSs [20, 22, 74, 99, 107–109]. Figure 3(c) shows a typical diffraction contrast TEM image of a Si/SiO_x NW HS grown by PLD [20]. An Fe_2O_3 shell was grown on vertically aligned Si NWs using the ALD process to form a dual-absorber system [82]. Yu *et al* prepared a Si NW/TiO_2 radial HS array with a CVD-grown TiO_2 layer on MACE-grown Si NWs for visible-light photocatalytic application [79, 80]. Yenchalwar *et al* [81] used a solution-based process to form a Si NW/TiO_2 HS, while Hwang *et al* [72] adopted a PLD technique to deposit a TiO_2 layer on the Si NW arrays using $TiCl_4$ and pure water as the precursors for the photocatalytic water splitting.

Multilayer core–shell structures based on a Si NW core have also been studied extensively for applications in multijunction solar cells, photocatalysts and LEDs [51, 65, 67, 68, 122, 123]. Katiyar *et al* have grown a Si NW/ZnS/AZO radial HS by PLD of ZnS and Al-doped ZnO (AZO) on MACE-grown Si NWs [65]. Figure 3(d) shows TEM images of a Si NW/ZnS/AZO core–shell HS with a Si NW core diameter of ~100 nm covered with an ~80 nm ZnS layer followed by a ~20 nm AZO layer [65]. Si NW/CdSSe complex HSs were formed by thermal evaporation of CdS and CdSe powder on Si NWs for applications in multicolor nanoscale LEDs [124]. Kargar *et al* [122] studied Si NW/

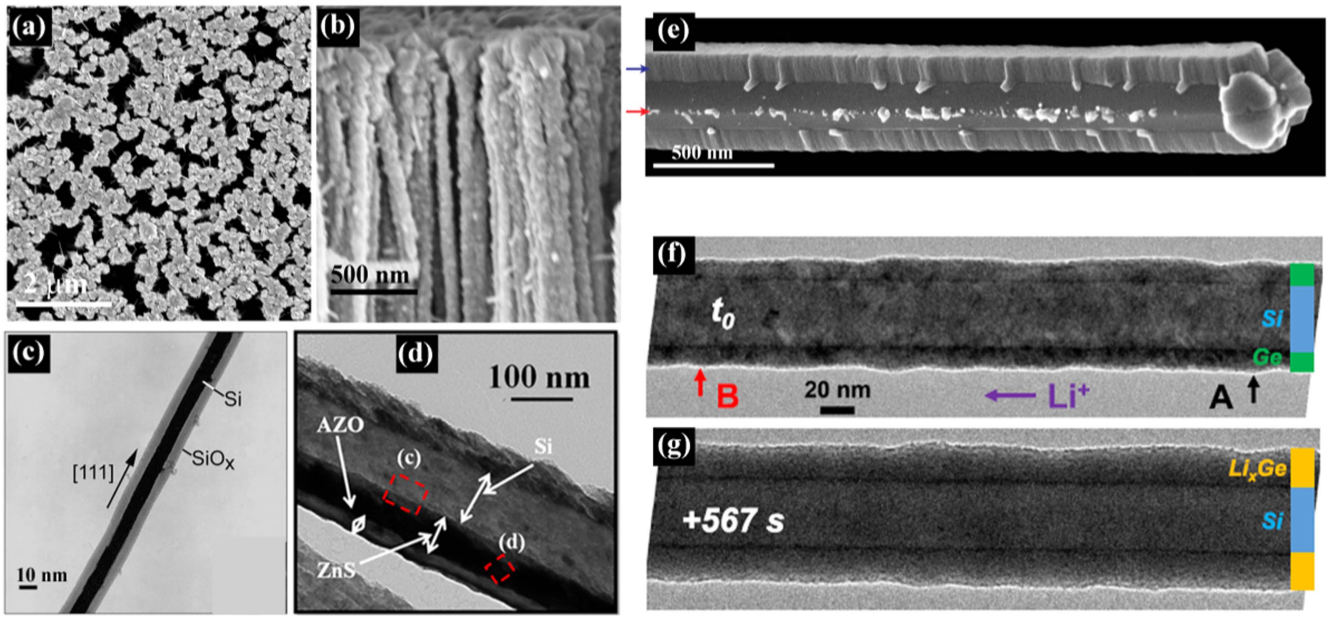

Figure 3. FESEM (a) top-view and (b) cross-sectional-view images of the Si NW/ZnO core–shell HS showing the rough surface of a Si NW due to ZnO coating on Si NWs [74], copyright 2015 Elsevier BV. (c) Diffraction contrast TEM image of a Si/SiO_x NW HS; crystalline material (the Si core) appears darker than amorphous material (SiO_x sheath) [20], copyright 1998 AAAS. (d) TEM images of Si NW/ZnS/AZO core–shell HS showing ~100 nm Si core, ~80 nm ZnS, and ~20 nm thick AZO layers [65], copyright 2014 American Chemical Society. (e) SEM image of a Si NW/CdS HS. The blue and red arrows indicate CdS on Si(111) and (110) facets, respectively [113], copyright 2015 American Chemical Society. (f), (g) *In situ* TEM observation for lithiation of a Si/Ge core–shell nanowire HS [115], copyright 2015 Nature Publishing Group.

SnO_2/Fe_2O_3 core–multishell HS photocathodes for neutral pH water splitting, while Wang *et al* [123] used an Al_2O_3/TiO_2 dual-layer passivation stack grown by ALD on Si NWs for efficiency enhancement of nanotextured black Si solar cells. InP- and CdS-coated Si NW photodetectors and solar cells were studied by different groups [112, 113]. CdS and InP shells, which are prototypical II−VI and III−V compounds, have been grown on Si NWs with well defined facets by a three-zone PVD process. A Si NW with well developed facets and diameters in the range 200–400 nm is shown in figure 3(e) before and after CdS growth. The blue and red arrows indicate CdS on Si(111) and (110) facets, respectively [113]. Liu *et al* fabricated a Si NW/Ge core–shell HS as a Li-ion battery anode. Figures 3(f) and (g) show the *in situ* TEM observation for lithiation of a Si/Ge core–shell nanowire HS [115].

In recent years, the photophysics of the Si NW/organic hybrid structures has been intensively studied to understand the charge separation and energy transfer processes. PEDOT:PSS, TAPC, P3HT, PDEF and TMAH are the commonly used organic materials for the fabrications of Si NW HS solar cells [69–71, 84, 85]. However, overall efficiency and long-term stability are major issues for the organic semiconductor-based solar cells. Core–shell Si NW HSs based on different carbon materials, such as graphene, graphite, RGO and CNTs, have also been utilized for different nanotechnology applications [39, 87, 116–120]. The nonuniformity in the shell thickness may deteriorate the performance of the core–shell NW HS-based devices.

2.3. Axial nanowire heterostructures

Besides the core–shell HSs, 1D NW axial HSs with well defined and controlled heterojunctions between different materials have recently become potential building blocks for future high-performance nano-optoelectronic and nanoelectronic devices. Both straight and kinked axial HSs with different materials have been studied on Si NWs. Si/Ge axial HSs have been grown by different groups [34–38, 127]. Axial Si/Ge NW HSs provide distinct advantages in electron transport applications, such as in FETs, by combining the smaller bandgap and higher carrier mobility of Ge while maintaining a more suitable current switching and subthreshold swing due to Si [127]. In most cases, Si/Ge axial HSs are formed by the VLS method using noble metal catalysts. Hybrid axial HSs, including integration of III–V semiconductors with Si technology, potentially have very interesting functionalities towards photovoltaic applications [33]. GaP–Si, GaP–Si–GaP and GaP–Si–GaP–GaAs–GaP–Si (hybrid Si/GaAs) NWs have been grown via the VLS process [33]. Kim *et al* fabricated wafer-scale Si NWs/graphene HSs for molecular sensing [39]. Single-layer graphene was fabricated by a CVD method and then transferred onto a vertically aligned and high-density Si NW array grown by MACE [39]. Si NW axial HSs based on other III–V and II–VI semiconductors, such as CdS [30] and InAs [32], have also been studied for different device applications. Metal silicide axial HSs, including MnSi [31], InSi [128], NiSi [129], Ni_2Si [129], PtSi [129], Pt_2Si [129] etc, have found applications as Ohmic interconnects in CMOS fabrication, LEDs, and

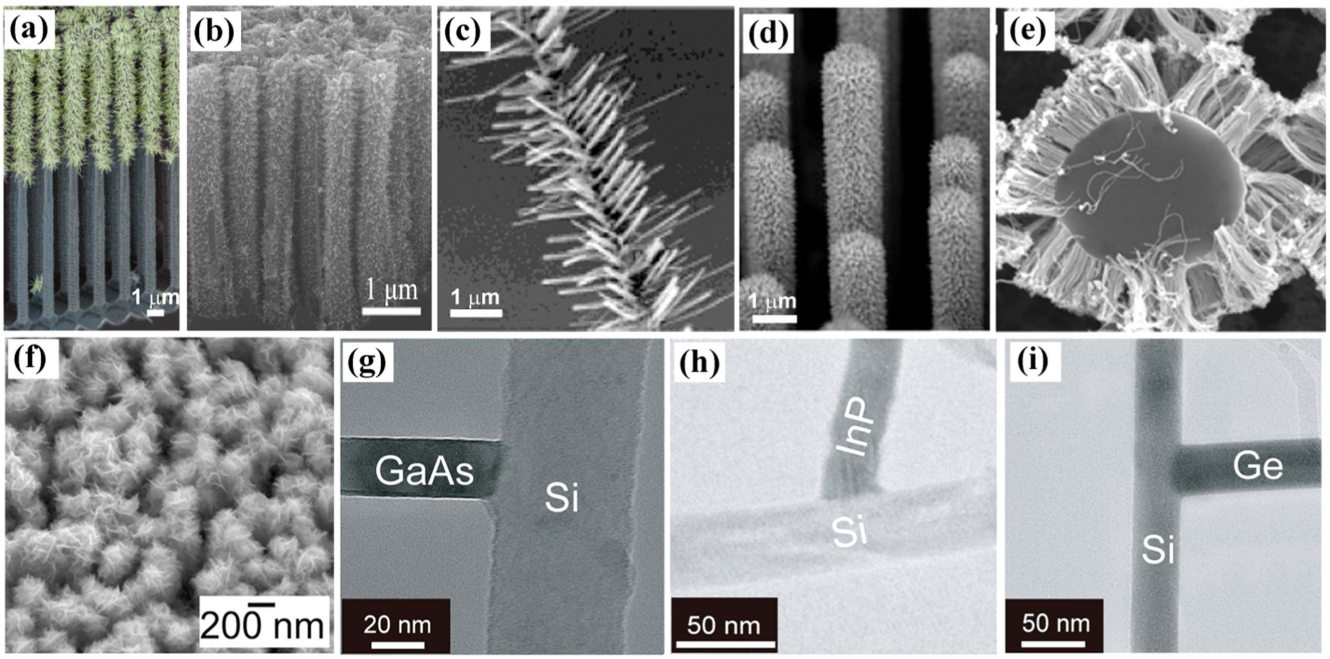

Figure 4. (a) SEM image of a Si NW–TiO_2 nanotree array [53], copyright 2013 American Chemical Society. (b) FESEM cross-sectional-view image of low-density ZnO branched Si NW–ZnO HSs [59], copyright 2015 American Chemical Society. (c) SEM images of a branched Si NW–GaN HS using 0.1 M nickel catalyst precursor solution [57], copyright 2004 American Chemical Society. (d) Tilted (45°) SEM images of hierarchical Si–$In_xGa_{1-x}N$ nanowire arrays on Si(111) substrate with $x = 0.08$–0.1 [52], copyright 2015 American Chemical Society. (e) SEM image of Si–Au branched NW HSs [131], copyright 2013 American Chemical Society. (f) SEM image of Si–Co NW HSs [132], copyright 2013 American Chemical Society. TEM images of branched (g) Si–GaAs, (h) Si–InP and (i) Si–Ge NW HSs [56] (Jianga X *et al* 2011 *Proc. Natl Acad. Sci. USA* **108** 12212).

inexpensive thermoelectric and photovoltaic devices. Besides the axial NW HSs, side-to-side Si–ZnS [40], Si–ZnSe [40], Si–ZnO [42] and Si–CdSe [41] biaxial NW HSs and sandwich-like ZnS–Si–ZnS [40] and ZnO–Si–ZnO [42] triaxial NW HSs have also been studied. The universal requirement of axial HSs for device applications is straight NW structures. However, kinking is a common problem during the growth of Si NW axial HS.

2.4. Branched nanowire heterostructures

As compared to 0D NPs and 1D NWs, 3D branched NW (nanotree, nanoforest and hierarchical NW) HSs present an additional degree of freedom to enable greater functionality, increased surface area and direct electron transport pathways. The essence of this idea is the control over the density and size of the nanoscale branches on the Si NW backbone, which ultimately enables the rational design of building blocks. A variety of 3D branched Si NW HSs have been developed to utilize their distinct properties for emerging applications in photovoltaics, photocatalysis, photoelectrochemical water splitting, supercapacitors, Li-ion batteries etc. Several 3D branched Si NW-based HS systems have been studied, including oxide semiconductors, such as Si/ZnO [51, 59–61, 130], Si/TiO_2 [50, 53–55], Si/SiO_2 [58], group IV semiconductors, such as Si/Ge [56], III–V semiconductors, such as Si/InP [56], Si/GaN [57], Si/GaAs [56], Si/GaP [56], Si/InGaN [52], II–VI semiconductors, such as Si/CdS [56], metals such as Si/Au [131], metallic silicide and alloys, such as Si/Au [56], Si/Co [132] etc. Figure 4 shows a glimpse of different types of branched Si NW HS reported in the literature. In most cases, a sequential catalyst-assisted growth technique was adopted for the fabrication of the branched HSs. The process contains three steps: standard Si NW growth as the backbone, followed by the deposition of metal catalyst onto the NWs, and finally VLS or SLS growth of the branched NWs onto the Si NW backbone. This method allows a good control on the density, size and length of the branches by adjusting the catalyst size and the interparticle distance. However, both VLS and SLS have advantages and drawbacks. The former (VLS) provides a good control on the branches and ordering, but requires high temperatures and sophisticated growth facilities. The latter (SLS) can take place at low temperatures with high yield. It enables the production of branched nanostructures with a rich variety of morphologies easily by adjusting the precursor solution and preparation conditions. However, in most cases the branches have no alignment and are randomly oriented and suffer from poor crystal quality. From the application point of view, 3D branched Si NW HSs are mostly exploited in the emerging area of energy conversion and storage. However, further development in this area requires improvement in synthetic methods and novel fabrication processes to provide better control of the structural quality, composition uniformity, surface chemistry and interface properties.

2.5. Nanoparticle-decorated nanowire heterostructures

Decoration of metal and semiconductor NPs on Si NWs has been carried out mainly for the improvement of the sensing,

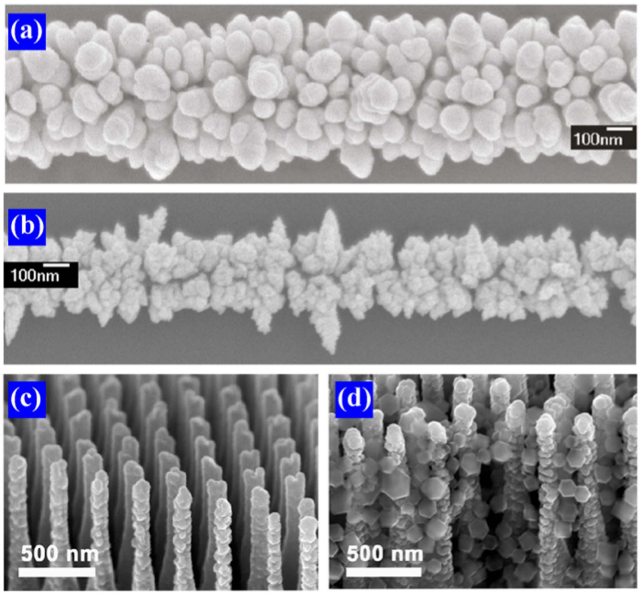

Figure 5. (a), (b) SEM images of Si NWs decorated with Ag (a) and Au (b) NPs [45], copyright 2009, American Chemical Society. (c), (d) SEM images of TiN–Ti–Si NR (c) and ZIF-8–TiN–Ti–Si NR (d) HSs [125], copyright 2016, American Chemical Society.

photocatalytic, luminescence and photovoltaic properties. The NP loading is usually performed by an *ex situ* deposition through a solution, PVD or CVD process on the Si NWs. Sun *et al* deposited ZnO NPs on MACE-grown Si NWs by a typical metal–organic CVD process [73]. Chen *et al* fabricated CdSe-decorated Si NWs for improved photodetection and photocatalytic performance [133]. Xie *et al* reported a Si NW array–carbon quantum dot (CQD) core–shell HS photovoltaic device by directly decorating CQDs using spin coating on MACE-grown Si NWs [43]. Si NW HSs decorated with different metal NPs have been reported owing to their surface plasmon resonance (SPR)-modified optoelectronic properties, excellent photocatalytic nature under visible-light illumination and outstanding SERS sensitivity. In most cases, the metal NPs were loaded on the Si NW surface by an electroless deposition technique using chemical solution. A variety of metal NPs, such as Ag, Au, Pt, Pd, Cu and Co, have been decorated on Si NWs by dipping the Si NWs into a solution containing HF and $AgNO_3$, $HAuCl_4$, H_2PtCl_6, $PdAc_2$, $Cu(NO_3)_2$ and $Co(NO_3)_2$, respectively [45]. Figures 5(a) and (b) show SEM pictures of the Ag and Au NP-decorated Si NWs [45]. Mixtures of HF and $AgNO_3$, $AuCl_3$, $PtCl_2$, $PdCl_2$, $RhCl_3$ and $CuCl_2$ have been used to decorate Ag [17], Au [17, 48], Pt [17], Pd [17, 48], Rh [17] and Cu [134] NPs, respectively, on Si NWs for photocatalytic application. Thermal evaporation techniques have also been utilized to decorate the metal NPs on the Si NWs [47]. Interestingly, Si NWs decorated with bimetal NPs, such as Au–Pd or Pd–Ni, exhibited superior properties as compared to the case of single-metal NP decoration. Sometimes the NPs are coated on radial and branched HSs of Si NWs to improve the device performance [81, 135]. Yenchalwar *et al* fabricated Au NP-decorated Si NW–TiO_2 HSs by a chemical process [81]. Sudhagar *et al* fabricated high-open-circuit-voltage QD-sensitized solar cells by decorating CdS and CdSe NPs on Si NW–ZnO branched HSs through a solution process [49]. Zeolite imidazolate framework-8 (ZIF-8) NPs embedded in Si NW–Ti–TiN without pyrolysis have shown increased energy storage capacity as anodes for lithium ion batteries (LIBs) [125]. Figures 5(c) and (d) show SEM images of TiN–Ti–Si NRs before and after ZIF-8 NP decoration [125]. Duan *et al* demonstrated Si NW–PEDOT–Ag NP HSs as an efficient and stable photocatalyst [136].

2.6. Functionalized nanowire heterostructures

The native oxide layers present on the surface of Si NWs often limit the performance of devices based on Si NWs. In order to remove the effect of oxide layers and the interface defects, the Si NWs can be functionalized chemically to improve the device performance. These functionalized Si NWs can be treated as an HS, and this has a huge impact on the Si NW-based sensor, photocatalysis and photovoltaic devices [17, 109, 134, 137]. The surface modification and functionalization have been carried out mainly by chemical processes. Yuan *et al* tuned the electrical properties of Si NWs by creating H-terminated Si NWs [138]. A Si NW-based pH sensor has been demonstrated by modifying the NW surface with 3-aminopropyltriethoxysilane (APTES), which produces amino groups as well as Si–OH groups [139]. To modify the Si NW surfaces with cyano groups, the Si NWs were immersed in an anhydrous toluene solution of (3-cyanopropyl)trichlorosilane (1%), followed by rinsing in anhydrous toluene and ethanol. The Si–CN NWs were hydrolyzed in aqueous H_2SO_4 to obtain Si–COOH NW HSs [140]. $-CH_3$, $-C_6H_5$, $-COOH$ and $-COOCH_3$ functional groups have been attached to the Si NWs for sensing of volatile organic compounds (VOCs) [141]. Hydrogen-terminated Si NWs, i.e. Si–H NWs, have been prepared by dipping the Si NWs into a HF solution, and these Si–H NWs show excellent photocatalytic activity as compared to the bare Si NWs [17, 109, 134, 137]. 3-mercaptopropyl-trimethoxysilane (MPTMS), (3-glycidoxypropyl)-methyl-diethoxysilane (GPTS) and (3-bromopropyl)-trichlorosilane have been reported to introduce thiol, epoxy and bromide terminal groups, respectively, on Si NWs [142]. Different C3 alkyl groups, specifically propyl ($Si–CH_2–CH_2–CH_3$), propenyl ($Si–CH{=}CH–CH_3$), and propynyl ($Si–C{\equiv}C–CH_3$), are used to functionalize Si NWs in order to improve the sensing performance of the Si NWs [143]. These functionalized Si NWs with different surface states open a new window to rationally design photoactive materials for various photoactive reaction systems. In some cases, Si–Si NW homojunction HSs with different doping types have also been utilized for applications in photovoltaics [2, 6, 8, 15, 144].

3. Energy conversion and storage applications

Based on the improved optoelectronic properties of the Si NW HSs, possibilities for efficient applications of Si NW HS-

based devices in energy conversion and storage applications are being investigated extensively and various model devices have been fabricated to demonstrate the superiority of the Si NW HSs over the bare Si NW-based devices. In this section, we will briefly discuss some of the important energy applications of Si NW HSs including the novel properties, limitations of the existing approaches, strategies for performance improvement and problems in its commercialization.

3.1. Light emitting diodes

Light-emitting diode (LED) lights are one of the latest inventions for reducing energy consumption and to minimize the negative effects of conventional bulbs to the environment. Studies reveal that LED bulbs produce less carbon than older bulbs, which can be very useful to get rid of the ill-effects of global warming. Traditionally, compound semiconductors with direct bandgap have been mostly exploited for the fabrication of LEDs. Despite Si having an indirect bandgap, Si NWs can emit light at room temperature with tunable wavelengths depending on their size, doping and surface conditions [22, 103, 107–109, 145–148]. Various mechanisms, including the quantum confinement (QC) effect and surface state or defects, have been proposed for the origin of light emission, though this is an ongoing debate [22, 103, 107–109, 145–148]. The light-emitting properties of the Si NWs can be enhanced with tunable color by creating HSs with suitable materials in appropriate configurations [65, 149–152]. However, most studies to date have been dedicated mainly to the fundamental understanding of the light emission from Si NWs and its HSs, rather than to real-world applications, such as LEDs. The main reason behind the same is the low quantum yield (QY) of the Si nanostructures and their HSs. For example, the QY for Si QDs, Si NWs/NCs, Si NWs and Si NW–ZnO HSs were 10%, 0.1%, 2% and 0.8%, respectively, which are much lower than the QYs of other direct bandgap semiconductors [109, 153–155]. In recent years, Si NW-based hybrid LEDs have shown promising improvement in the PL and electroluminescence (EL) efficiencies as compared to the bare Si NW LEDs and other hybrid LEDs [65, 149–152]. A variety of materials including semiconductors, metals and dielectrics have been tested for the enhancement and tuning of PL and EL properties of Si NWs and other kinds of Si nanostructure [65, 73, 74, 81, 149–151, 153]. PL and EL properties of Si NW–ZnO HSs have been studied extensively in the last decade [73, 74, 149–151, 153]. In most cases, n-type ZnO is deposited on p-type Si NWs/NRs to form a core–shell structure or ZnO NC-decorated p–n junction hybrid LED. The increased surface area resulting from the enhanced structural aspect ratio and the antireflective characteristics inherent to the NW structure were believed to be responsible for the large enhancement in emission intensity in most cases [108, 151]. Sun *et al* fabricated Si NW–ZnO core–shell and ZnO QD-coated Si NWs by a CVD method and demonstrated that in presence of ZnO the PL spectra of the HS covered the entire visible region (400–800 nm), which is important for the fabrication of white light LEDs [73]. Si nanotip–ZnO and nanoporous Si NW–ZnO p–n junction LEDs were studied by means of EL [149, 153]. Room-temperature EL was observed under a broad range of applied voltages. However, the QY was quite low (0.008) in this case [153]. SiC-coated Si NWs showed threefold enhancement in the PL [114]. The PL intensity of the Si nanostructure is usually enhanced by incorporating metal NPs. The highest reported PL intensity enhancement of Si NWs in the presence of nanoscale Ag island arrays was fourfold [106], while it was threefold enhanced in the case of Au islands [156]. The enhancement in PL efficiency was explained in terms of radiative energy exchange between Si and metal NPs due to enhanced exciton–plasmon radiative coupling [103, 109, 156]. Enhanced PL and photoactivity was observed from plasmon-sensitized n-Si NW–TiO_2 HSs [81]. Faro *et al* demonstrated Si NW–CNT flexible HSs, which exhibited the unique feature of a simultaneous photon emission at room temperature both in the visible (owing to NWs) and in the IR (owing to CNTs) regions [121].

Solid-state white light sources are in great demand for future day-to-day lighting applications. Si NW HS-based broadband white LEDs have been successfully demonstrated [65, 149, 152]. Si–ZnO NW HSs are considered a potential light source for future solid-state white LED devices [149, 153]. Katiyar *et al* fabricated Si–ZnS radial NW HS arrays for a white LED on Si substrate [65]. Figure 6(a) shows a schematic diagram illustrating the coaxial Si NW–ZnS–AZO radial HS LED device [65]. The white light emission could directly be observed by the naked eye when sufficient forward bias was applied across the device with AZO as the cathode and Al as the anode. The EL spectra of Si–ZnS radial heterojunction arrays at different applied biases in the range of 2–13 V are shown in Figure 6(b) [65]. The LED performance was excellent within a broad range of temperature (10–400 K) [65]. Moon *et al* demonstrated a white light LED based on surface-oxidized porous Si NW arrays and amorphous In–Ga–ZnO capping [152]. Figure 6(c) shows the deconvoluted EL spectra of the Si NW–a-IGZO LED under 8 V forward bias. EL microscopy images in figure 6(d) of the HS LED confirm that the EL image consists of many small emission spots having different colors, such as blue, green, yellow, orange and red, and the brightness increases with higher applied voltage [152]. Recent studies have been devoted to fabricating Si NW-based LED heterostructures with different plasmonic metals, group IV, II–VI and III–V semiconductors, organic semiconductors etc. However, the quantum efficiencies QY of the devices are not up to the expected standard and more studies are needed on the design and optimization of the LED structures.

3.2. Solar cells

Solar cells, which directly convert solar energy into electricity, offer the most acceptable and stable solution to the challenges of meeting the growing global energy demand. Among current solar cell technologies, Si-based solar cells are the most popular, dominating over 80% of the market due to their high efficiency, long-term stability, abundant material resources and well established fabrication techniques. To

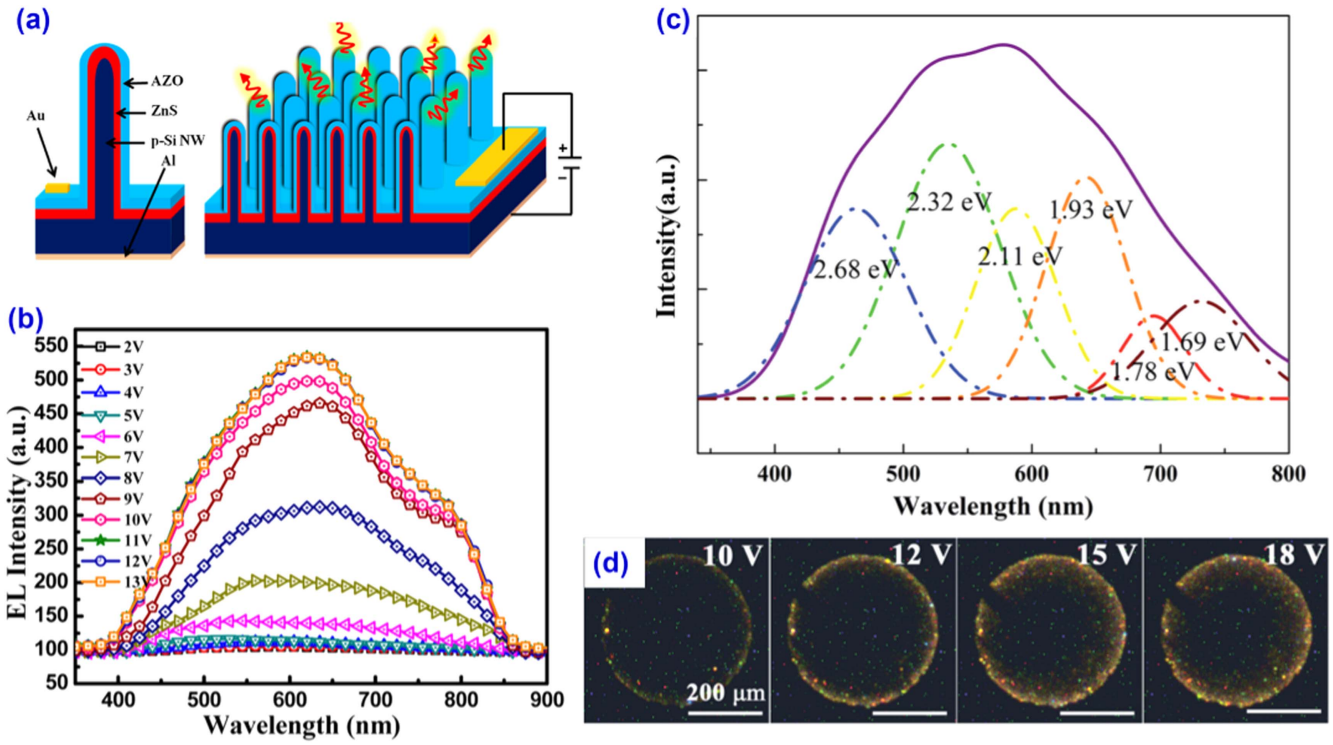

Figure 6. (a) Schematic diagram illustrating core–multishell Si NW–ZnS–AZO HS LEDs. (b) Room-temperature EL spectra of Si NW–ZnS radial HS arrays under different forward biases [65], copyright 2014 American Chemical Society. (c) EL spectra with deconvoluted subpeaks obtained from the Si NW–a-IGZO LEDs. (d) EL microscopy images of the white light emission from Si NW HS LEDs [152], copyright 2014 Royal Society of Chemistry.

Table 1. Summary of the reported high-performance Si NW HS-based solar cells including the HS components, HS type, fill factor (FF) and photoconversion efficiency (PCE) of the respective solar cells.

NW heterostructure components	Heterostructure type	Si NW growth process	FF (%)	PCE (%)	References
p-Si/n-Si NW	core–shell	RIE	60.7	5.3	[64]
p-Si/n-Si NW	core–shell		60.0	7.53	[163]
Si/Si NW	core–shell	CVD	65.4	7.9	[62]
Si NW/Si	core–shell	MACE	65.1	9.3	[158]
a-Si:H/a-Si:H/c-Si NW/a-Si:H/a-Si:H	core–multishell		81.0	12.4	[159]
Si NW/graphene	axial		66.0	7.7	[117]
Si NW/P3HT/graphene	core–shell		55.2	10.3	[116]
Si NWs/CNT	branched		76.0	15.1	[160]
Si NW/Carbon Q-dot	NP decorated		59.3	9.1	[43]
Si NW/SiN_x	core–shell		79.2	17.8	[111]
Si NW/Al_2O_3	core–shell		78.7	22.1	[110]
Si NW/Al_2O_3/TiO_2/FGA	core–shell		79.9	18.5	[123]
Si NWs/ZnO NRs	branched		67.7	10.5	[130]
Si NW/Pt NPs	NP decorated		61.0	8.14	[44]
Si NW/Carbon/Pt	NP decorated		55.5	10.9	[135]
Si NW/P3HT	core–shell		54.0	9.2	[70]
Si NW/PEDOT:PSS	core–shell		64.2	11.6	[69]
Si NW/TAPC/PEDOT:PSS	core–shell		67.1	13.1	
Si NW/Alq3/PEDOT:PSS	core–shell		68.2	11.9	[161]
Si NW/OXD-7/PEDOT:PSS	core–shell		69.9	12.9	

meet the key issues related to the Si nanostructure-based photovoltaics, i.e. photon absorption, exciton transport, exciton dissociation/charge separation, charge collection etc, Si NW HSs have drawn considerable attention. Table 1 summarizes the recent progress in the performance of the Si NW HS-based solar cells. Due to the superior photovoltaic

properties of MACE-grown Si NWs over the NWs grown by other methods [157], much attention has been paid to choose appropriate material(s) for forming HSs with MACE-grown Si NWs in order to improve the photovoltaic performance.

The photovoltaic performance of the Si NW-based radial and axial p–n homojunction HSs has been studied by different groups. Among several growth strategies, MACE-grown Si NWs show the best photoconversion efficiency (PCE) due to their ultra-low reflectivity over the entire range of wavelength, which arises from the multiple reflections on the inner surface of the vertical Si NW array and a broad range of size distribution of the Si NCs on the surface [158]. The importance of good electrical contact, passivation of the surface and interface defects to reduce the carrier recombination to improve the performance of Si NW-based solar cells were eventually realized. By using an a-SiN:H layer to passivate the Si NW surface, Kim *et al* showed that the PCE of the solar cell could be improved significantly from 7.2% to 11.0% due to the increased light absorption and improved charge-carrier collection [162]. Surface/interface recombination and high series resistance are some of the key issues for the low efficiencies. Very recently, Lin *et al* demonstrated a high-performance Si NW-based solar cell through surface passivation by using SiO_2 and SiN_x, and the PCE was 17.75% [111]. Ultralow average reflectance of 4.93% and low effective surface recombination velocity of 6.59 m s^{-1} were believed to play crucial roles in the high performance. Ko *et al* recently demonstrated that a simple change in the morphology of Si NWs can improve the PCE [163]. From both numerical simulation and experiments, it was shown that the PCE can be improved from 5.26% to 7.53% by simply changing the Si NW structure from a conventional symmetric to an asymmetric nature, that leads to increased J_{SC} [163]. To improve the photovoltaic parameters of Si NW-based solar cells, p–i–n and tandem p–i–n^+–p^+–i–n junction Si NW solar cells were also studied, though the performance was not impressive [144]. Togonal *et al* fabricated p–i–n–i–n^{++} heterojunctions based on ITO-coated a-Si:H–a-Si:H–c-Si NW–a-Si:H–a-Si:H and achieved a PCE of 12.43% [159]. A schematic diagram of the HS solar cell and its SEM cross-section image are shown in figure 7(a). The authors tuned the thickness of the a-Si:H (p type) and a-Si:H (i type), and realized a PCE improvement from 4.13% to 12.43% (A, B, C, D, E and F cells with thicknesses of 14, 28, 32, 48, 64 and 80 nm, respectively). The external quantum efficiency (EQE) and the *J*–*V* curves for the different types of cell are displayed in figures 7(b) and (c). J_{SC}, fill factor (FF) and PCE achieved a good performance at the optimal a-Si:H thickness of 32 nm [159]. Lin *et al* fabricated a Schottky junction-based Si NW–graphene solar cell by transferring the CVD-grown graphene onto a Si NW array [117] and reported a maximum PCE of 7.7%. The authors studied the cell performance theoretically and concluded that, by controlling the graphene layer number, tuning the graphene work function and adding an antireflection film, a maximal theoretical PCE of 9.2% could be achieved [117]. Zhang *et al* experimentally found that four layers of graphene exhibits the best performance, because the transmittance is reduced when the number of graphene layers is higher than five [116]. The authors further showed that, by inserting a P3HT conductive polymer (10 nm) as an electron-blocking layer, a maximum PCE of 10.3% could be achieved [116]. Si NW–carbon QD heterojunctions with a barrier height of 0.75 eV exhibited excellent rectifying behavior with a rectification ratio of 10^3 at $\pm$0.8 V in the dark, and PCE as high as 9.1% under AM 1.5 G irradiation was achieved. It was believed that such a high PCE came from the improved optical absorption as well as the optimized carrier transfer and collection capability [43]. Feng *et al* studied branched ZnO NRs on Si NWs for solar cell application [130]. Figure 7(d) shows a schematic representation of the Si NW–ZnO branched HS solar cell and the corresponding SEM image of ZnO NR branches on the Si NWs. The existence of the ZnO NRs drastically decreases the reflectivity of the HS samples from 25% to about 10%, especially in the wavelength range < 400 nm. The internal quantum efficiency (IQE) of Si NW solar cells with ZnO NRs is higher than the other combinations, especially in the short-wavelength range, as shown in figure 7(e). In the HS sample, the J_{SC} improves from 22.5 to 27.9 mA cm^{-2} (figure 7(f)). The FF increases from 56.3% to 67.7% and the efficiency improves from 9.2% to 10.8%. The efficient carrier collection and enhanced photon absorption caused by the ZnO NRs are thought to be responsible for the observed improvement [130]. CdS, CdSe QD-sensitized branched Si–ZnO NWs [49] and hierarchical p-Si–n-CdS–n-ZnO nanoforest HSs [164] have also been studied. However, the overall efficiency was not impressive.

In order to increase the efficiency, passivation of the dielectric coating is the conventional method of reducing the surface recombination rate by decreasing the interfacial state density. Field-effect passivation (the built-in electric field reduces the minority-carrier concentration near the interface) has also been adopted in some cases. Al_2O_3 is commonly used to suppress the Auger and surface recombination significantly via field-effect passivation. Recently, Wang *et al* fabricated solar cells consisting of Si NW arrays and an Al_2O_3–TiO_2 dual-layer passivation stack on the n^+ emitter [123]. The Si NW–Al_2O_3–TiO_2 HS solar cell showed 11% increased short-circuit current density and an impressive 18.5% efficiency after performing forming gas annealing (FGA) [123]. Figure 7(g) shows a schematic diagram of the Si NW–Al_2O_3–TiO_2 HS solar cell with the n^+-emitter–p-base structure, along with the band diagram. The Al_2O_3–TiO_2 dual-layer passivation stack causes an enormous decrease in the total reflectance, which could be attributed to the refractive index gradient caused by the insertion of a low-refractive-index layer between the Si NWs and air [123]. Figure 7(h) shows the EQE of HS solar cells with different passivation layers. It is clear that all of the cells with surface passivation layers exhibited higher EQEs than cell 1 across the entire spectral range tested. The decreased surface recombination rate and reduced reflectance of the cells with surface passivation layers were responsible for the increases in EQE. The enhanced efficiency (18.5%) was attributed to the increased J_{SC} (figure 7(i)) that was caused by the decreased surface recombination rate, and the increased light absorption owing to the reduced total reflectance [123]. Savin *et al* fabricated

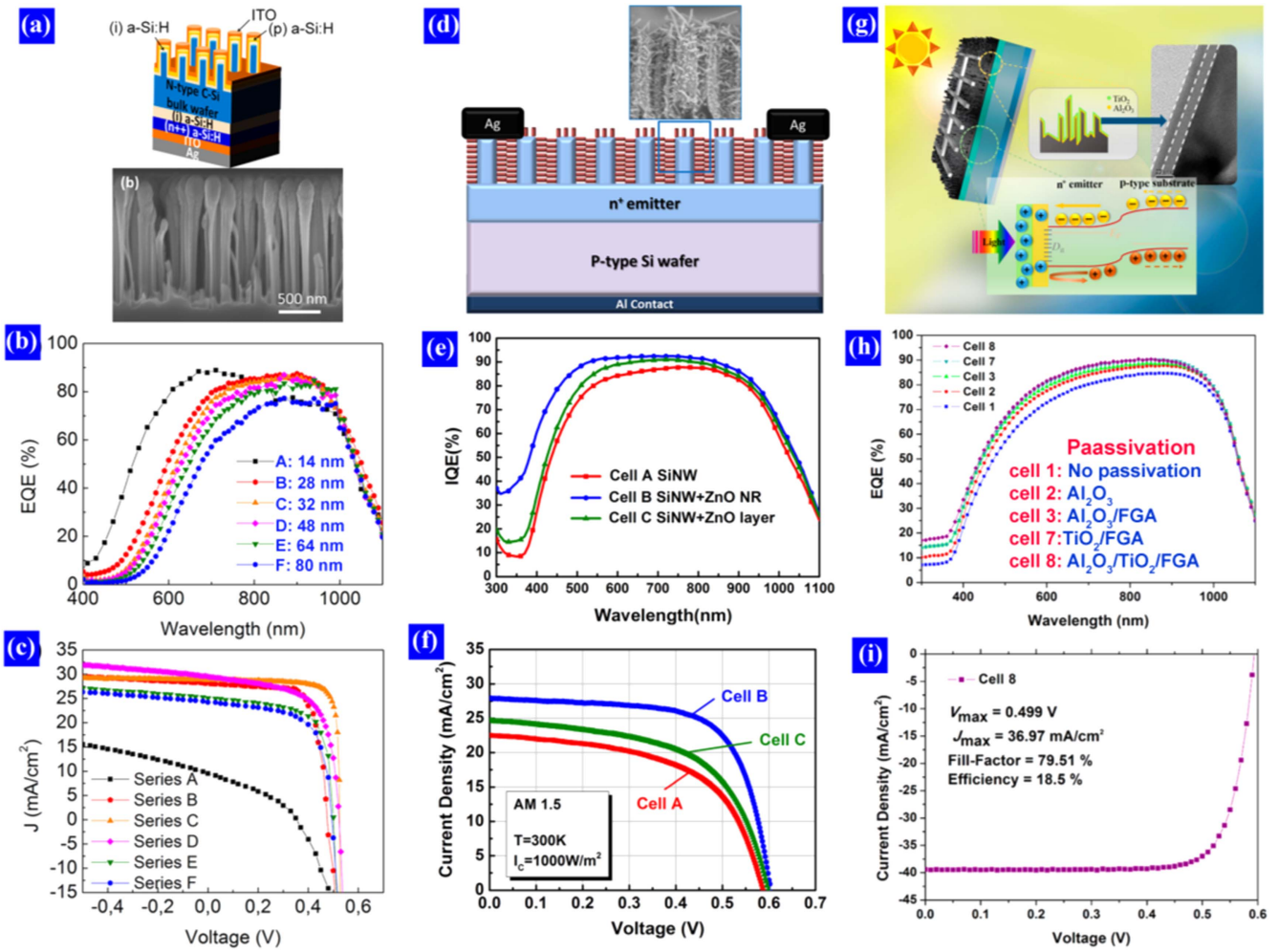

Figure 7. (a) Schematic diagram of the ITO-coated a-Si:H–a-Si:H–c-Si NW–a-Si:H–a-Si:H heterojunction solar cell (upper panel) and its SEM cross-section image (lower panel). (b) EQE and (c) *J–V* curves of the HS solar cell with different thicknesses of amorphous Si layer [159], copyright 2016 American Chemical Society. (d) Schematic diagram of the Si NW–ZnO branched HS solar cell and SEM image of ZnO NR branches on the Si NWs. (e) IQE and (f) *J–V* characteristics of the HS solar cells [130], copyright 2015 AIP Publishing LLC. (g) Schematic diagram of the Si NW–Al_2O_3–TiO_2 HS solar cell with the n^+-emitter–p-base structure, along with a band diagram. (h) EQE and (i) illuminated $J-V$ characteristics of the HS solar cell [123], copyright 2015 American Chemical Society.

remarkable >22% efficient solar cells with a surface area of 9.0 cm^2 [110]. The authors used an optimal surface reflectance without affecting the surface recombination, due to the outstanding surface passivation achieved with the conformal ALD-coated Al_2O_3 layer. Auger recombination was avoided by using a surface-sensitive 280 μm thick interdigitated back contact (IBC), where the junction and the contacts are placed at the back of the cell [110]. However, long-term stability of the cells is not addressed in most of the studies.

Recently, concerted efforts have been made to realize efficient Si NW-based organic HS solar cells in order to reduce the cost by adopting low-temperature, scalable, and soluble process of conjugated polymers, such as P3HT, poly (3, 4-ethylene dioxythiophene):poly-(styrenesulfonate) (PEDOT:PSS), 1, 1-bis[(di-4-tolylamino)phenyl]cyclohexane (TAPC), p-poly(9, 9-diethylfluorene) (PDEF), Tris(8-hydroxyquinolinato)aluminium (Alq3), 1, 3-bis(2-(4-tert-butylphenyl)-1, 3, 4-oxadiazol-5-yl)benzene (OXD-7) etc [69–71, 165]. However, the maximum PCEs obtained to date are 5.9%, 9.2% and 9.7% using PDEF [71], P3HT [70] and PEDOT:PSS [165] as the conjugated polymer, respectively. Very recently, 13.36% efficient Si NW–PEDOT:PSS solar cells have been fabricated by surface-modified Si nanotips using a chemical polishing etching method in order to remove the surface defects [85]. Yu *et al* fabricated 13.1% Si NW–TAPC–PEDOT:PSS organic solar cells by incorporating a thin layer of TAPC in between Si NWs and PEDOT:PSS [69]. Figures 8(a)–(c) illustrate the device configuration along with the device parameters with and without the intermediate TAPC layer [69]. The TAPC layer improves the morphology of the PEDOT:PSS layer on the Si NWs, while a large electron barrier suppresses the interface recombination and dark saturation current leading to an enhanced V_{OC} and FF [69]. Solar cells with the Alq3 and OXD-7 interlayers within the Si NW–PEDOT:PSS structure show notable enhancement in V_{OC} and FF, leading to a PCE up to 11.8% and 12.5%, respectively [161]. The role of the Alq3 or OXD-7 interlayer is equivalent to a thin interfacial oxide layer for the Al–Si

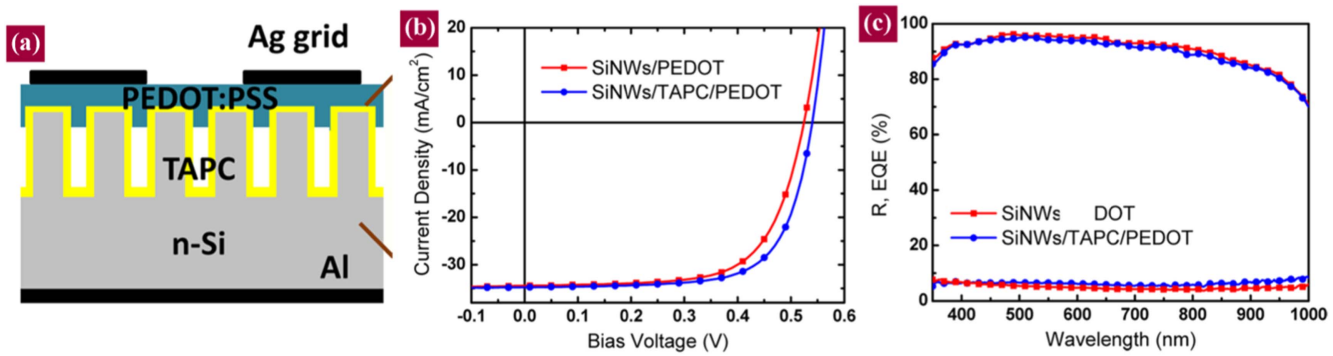

Figure 8. (a) Schematic diagram of the Si NW–TAPC–PEDOT:PSS heterojunction solar cell. (b) *J–V* characteristics of the hybrid solar cells under a simulated AM 1.5G illumination condition. (c) Reflectance (*R*) and EQE of the fabricated devices with and without the TAPC layer [69], copyright 2013 American Chemical Society.

Schottky barrier, instead of the interfacial doping. The existence of an interfacial oxide layer reduces the Schottky barrier height and increases the built-in potential, leading to a higher current at the turn-on condition than without the interfacial oxide [161].

In recent times, studies on Si NW HSs in low-cost liquid-state junction PEC solar cells have also emerged. Peng *et al* demonstrated a PEC solar cell consisting of vertical Si NW arrays, which exhibited remarkable photoactivity and photovoltaic properties in redox electrolyte containing HBR and Br [166]. A 3D NW architecture consisting of 20 μm long MACE-grown Si NWs and dense TiO_2 NRs yielded a PEC efficiency of 2.1%, which is three times higher than that of TiO_2 film–Si NWs having a core–shell structure [50]. However, such PEC solar cells still suffer not only from carrier recombination loss and poor carrier collection, but also from photocorrosion, and photooxidation of the Si NW surface, which lead to poor device performance and degradation. Wang *et al* showed that the PCE could be enhanced to 10.86% by incorporating a thin carbon layer in between the Pt NPs and Si NWs [135]. Very recently, NiO NPs were decorated on the Si NW arrays with a carbon shell to achieve a synergic effect of the catalytic activity in the PEC solar cell. The efficiency of the NiO@Si NW/C HS-based PEC solar cell was 9.49%, which was greater than that based on the Pt counter-electrode [167].

3.3. Thermoelectrics

Approximately 90% of the world's power is generated from thermal plants that use fossil fuel combustion as a heat source. The power conversion efficiency is typically 30%–40% and the rest of the 60%–70% thermal energy is lost to the environment [168]. Immense efforts have been devoted to recover the waste heat generated from various heating systems to a useful energy source by thermoelectric modules. However, widespread use of thermoelectricity as an alternative energy source has been hindered by the low figure of merit ($ZT = S^2\sigma T/\kappa$) of materials due to the correlation between the thermal conductivity (κ), Seebeck coefficient ($S = \mathrm{d}V/\mathrm{d}T$) and electrical conductivity (σ). MACE-grown Si NWs are currently attracting a great deal of interest as a promising alternative to commercial thermoelectric materials, such as bulk Bi_2Te_3, due to the increased *ZT* because of the reduced κ values for the rough Si NWs due to the enhanced phonon scattering at NW interfaces without affecting σ [168]. Hochbaum *et al* found that the MACE-grown Si NWs were much rougher than those grown by the VLS method, which resulted in five- to eightfold reduction in κ and enhanced *ZT*. The value of *ZT* of the Si NWs (~0.6) was two orders of magnitude higher than that of bulk Si due to the significantly reduced κ [168]. To improve *ZT*, attempts have been made to increase the value of σ by functionalization of Si NW surfaces chemically, without altering the value of κ. Li *et al* used NH_3 for the modulation of σ and showed that the value of σ is greatly increased after NH_3 adsorption on the surface of the Si NWs [169]. The enhancement of the electrical conduction was interpreted in terms of electron trap filling of the native oxide via NH_3 adsorption [169]. Lee *et al* reported a large improvement in *ZT* values, experimentally $ZT = 0.46$ at 450 K and computationally $ZT = 2.2$ at 800 K, from Si–Ge NW HSs [170]. The *ZT* improvement was attributed to the remarkable reduction in κ, which was thought to arise from the effective scattering of a broad range of phonons by alloying Si with Ge as well as by limiting the phonon transport within the NW diameters [170]. Recently, Yang *et al* theoretically predicted that a system of a Si NW core with a thin layer of Si–Ge alloy shell could provide an improved thermoelectric *ZT* [171]. Si NWs and their HSs are still less efficient than the current conventional thermoelectric materials, and researchers are optimistic about the improvement of *ZT* up to the commercial level at room temperature by further optimizing the size, morphology, surface and interface of Si NWs and their HSs.

3.4. Hydrogen production by photocatalytic water splitting

Utilizing solar energy through photocatalytic water spitting and production of hydrogen by semiconductor-based photocatalysts have received remarkable attention, as this holds a great potential to address the worldwide energy needs. Mainly wide bandgap semiconductors (e.g., TiO_2) are commonly used as photocatalysts because of their large bandgap and stability towards chemical and photochemical corrosion. To

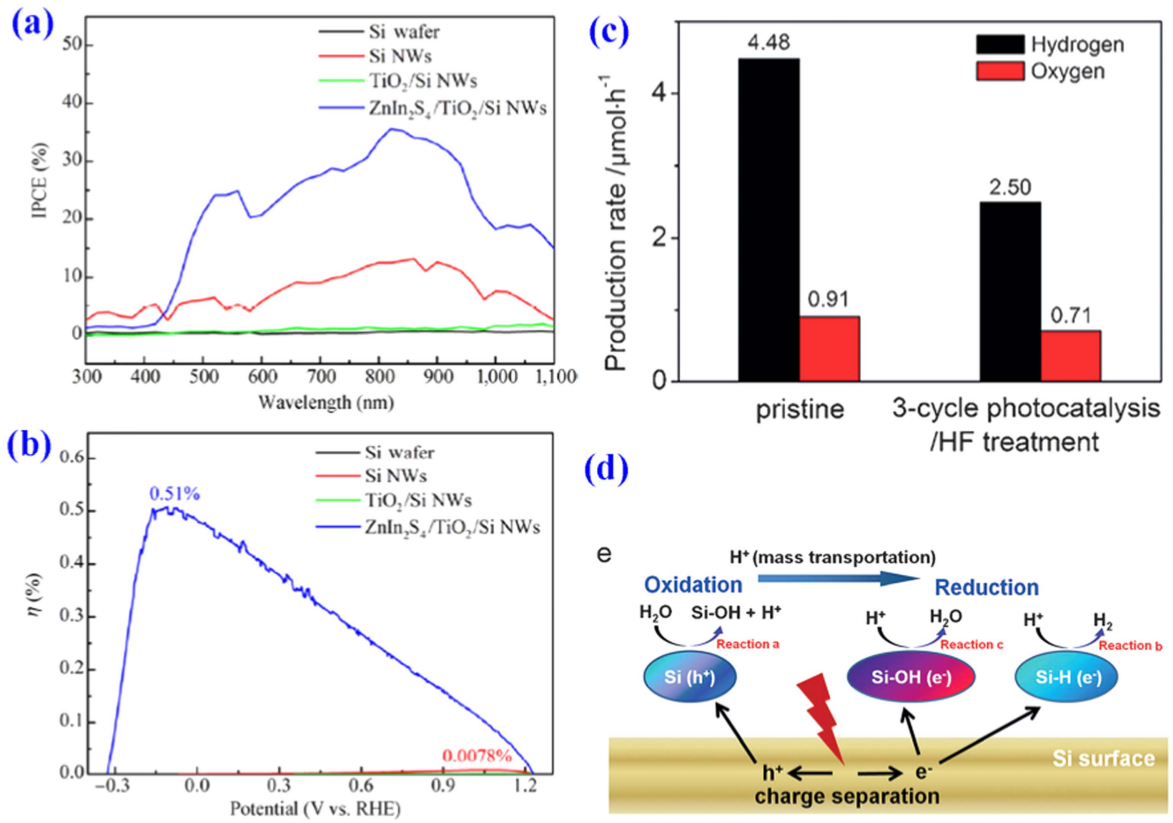

Figure 9. (a) IPCE spectra and (b) calculated conversion efficiencies as a function of the applied bias for the Si wafers, Si NW arrays, TiO_2–Si and $ZnIn_2S_4$–TiO_2–Si NW photoanodes [173], copyright 2015 Springer. (c) Photocatalytic H_2 and O_2 production from pure water under full-spectrum irradiation for 4 h, using the H–Si NWs and after three-cycle photocatalysis (HF treated). (d) A schematic diagram of the overall reaction mechanism for photocatalytic H_2 production on the Si surface [137], copyright 2015 John Wiley and Son.

overcome the serious drawbacks of fast charge recombination and the limited visible-light absorption in TiO_2, Si NWs and their HSs are being investigated with a great interest in H_2 production and fuel generation. Si NW HSs are also used as photocathodes and photoanodes in photoelectrocatalysis (PEC) and show excellent PEC activity in water splitting under UV–visible–NIR light illumination. The PEC water-splitting process involves the breaking of water molecules by a minimum of 1.23 eV energetic photons. Hence, a photoelectrode should absorb photons of light of energy larger than 1.23 eV, which also depends on the band edge positions of photoelectrodes to drive efficient water splitting. Branched NW HSs such as Si–TiO_2 [50, 54], Si–ZnO [61], Si–InGaN [52] and core–shell HSs such as Si–Fe_2O_3 [82], Si–SnO_2–Fe_2O_3 [122], Si–TiO_2 [72], Si–MoS_2 [172], Si–TiO_2–MoS_2 [172] and Si–TiO_2–$ZnIn_2S_4$ [173] have shown efficient PEC water splitting for the generation of clean H_2 fuel on a large scale via splitting of water into O_2 and H_2 under sunlight. Boettcher *et al* reported the use of radial n^+–p junction Si NW array photocathodes for PEC H_2 production from water [174]. It was demonstrated that high photovoltage, FF and IQE could be achieved after Pt NP decoration on the Si NW array photocathodes. The HS NW array photocathodes yielded energy conversion efficiencies $> 5\%$, while the bare Si NW array photocathodes yielded efficiencies $< 0.2\%$ due to the low photovoltage generated at the aqueous solution–p-Si junction [174]. Hwang *et al* investigated Si NW–TiO_2 HSs to determine their potentiality for the photooxidation of water. The HSs exhibited 2.5 times higher photocurrent density than the planar Si–TiO_2 due to lower reflectance and higher surface area [72]. A 3D branched NW architecture consisting of 20 μm long MACE-grown Si NWs and dense TiO_2 NRs yielded a PEC efficiency of 2.1%, which is three times higher than that of TiO_2 film on Si NWs having a core–shell structure [50]. Long optical path for efficient light absorption, high-quality 1D conducting channels for rapid e–h separation and charge transportation as well as high surface area for fast interfacial charge transfer and electrochemical reactions were believed to be responsible for the improved efficiency [50]. Si NW–ZnO branched HS photoelectrodes in PEC solar water splitting showed an order of magnitude enhancement in photocurrent as compared to the bare Si NW photoelectrodes. Long-term stability of the photoelectrode (unchanged photocurrent for over 24 h under constant light illumination) was achieved by coating a thin TiO_2 layer, and a biasing potential of -0.33 V (versus RHE) was achieved [61]. A MoS_2 layer-wrapped Si NW array photocathode was studied for H_2 evolution, and it provided a current density of ~15 mA cm^{-2} at 0 V versus RHE, indicating that this photocathode can be an affordable integrated water-splitting system [172]. The authors achieved a high current density with high stability after inserting a thin layer of TiO_2 in between the MoS_2 shell and Si NW core [172]. A novel multijunction photoelectrode was fabricated with Si NWs as cores, $ZnIn_2S_4$ nanosheets as

branches and a TiO_2 film as the sandwiched layer [173]. Figure 9(a) shows the incident photon-to-current conversion efficiency (IPCE) measured at 0.88 V versus RHE, while figure 9(b) shows the corresponding solar-to-H_2 conversion efficiency (η) for different configurations. This junction exhibited a superior PEC performance with a maximum photoconversion efficiency of 0.51%, which is 795 and 64 times higher than that of a bare Si wafer and Si NWs, respectively. The large enhancement was attributed to the effective e–h separation and fast excited carrier transport within the multi-junctions resulting from the favorable energy band alignments with water redox potentials, and to the enlarged contact area for facilitating the electron transfer at the multi-junction–electrolyte interface [173].

Since the PEC process requires a conducting substrate and a bias voltage, direct photocatalysis is a simpler and less expensive approach for H_2 production, fuel generation and environmental cleaning, despite its lower efficiency. Interestingly, Si NW HSs are drawing much attention in direct photocatalytic applications as compared to PEC. Liu *et al* produced H_2 and O_2 by simple pure water splitting by Si NWs grown by MACE under light illumination [137]. Figure 9(c) shows the photocatalytic H_2 and O_2 production from pure water under full-spectrum irradiation for 4 h using the H–Si NWs and after three-cycle photocatalysis (HF treated). It was argued that H_2 production occurs through the cleavage of Si–H bonds and the formation of Si–OH bonds. The overall reaction mechanism is depicted in figure 9(d). From the apparent quantum efficiency measurements, solar-to-chemical conversion efficiency of Si NWs was found to be comparable to those of many other visible-light photocatalysts [109, 137]. However, more studies are needed to realize its full potential for practical applications.

3.5. Artificial photosynthesis

The direct conversion of sunlight into energy stored in chemical bonds is termed artificial photosynthesis, which mimics the natural photosynthesis in plants. Typically solar light-driven water splitting to produce H_2 and O_2 and reduction of CO_2 for the production of hydrocarbon and other carbon-based organic fuels are involved in this process. Unlike photovoltaics, which aim to maximize power output, producing fuels from sunlight in PEC cells requires a minimum voltage output that is imposed by the chemical reaction involved. Additionally, electrochemical overpotentials need to be overcome to facilitate a high reaction rate [28]. Under the 'Z-scheme' approach, NW array electrodes can provide a reduced overpotential for solar to fuel conversion. They also provide the necessary photocurrent flux for practical applications, while maintaining a desirable voltage output [175]. TiO_2 is the most used electrode in PEC cells for artificial photosynthesis. Bare Si NWs and their HSs with different semiconductors such as TiO_2, ZnO, InGaN, Fe_2O_3, SnO_2/Fe_2O_3, MoS_2, TiO_2/MoS_2, Pt etc exhibit efficient PEC water splitting under sunlight for the production of clean H_2 fuel on a large scale [50, 52, 54, 61, 72, 82, 122, 137, 172–174]. p-type Si NWs were used as the photocathode, n-type TiO_2 nanotube film was used as the photoanode and saturated aqueous $NaHCO_3$ solution was used as the electrolyte in a PEC cell for the reduction of CO_2 [176]. C3–C4 hydrocarbons, methane, ethylene, CO, O_2 and H_2 were formed. Si–H NW photocathodes and Mn-based carbonyl bipyridyl complexes as homogeneous molecular catalyst were used for the reduction of CO_2 to CO in hydro-organic medium [177]. Liu *et al* used Si NWs for CO_2 photofixation with ketone-based substrates [178]. The reactions in the PEC cell produce organic targets that can be readily used for synthesis, such as ibuprofen and naproxen and ATP (adenosine-triphosphate) [178]. Although a lot of research is being carried out worldwide on the PEC process, Si NWs are less explored for this purpose. Effort should focus on the Si NW HS-based effective photoelectrodes that offer enhanced photocurrent and photoresponse, reduced turn-on potential, increased solar to fuel conversion efficiency, improved stability and most importantly property tunability.

3.6. Li-ion battery

Among various energy storage technologies, the rechargeable Li-ion battery (LIB) has received enormous attention owing to its amazing potential for energy storage applications, particularly in portable electronics and electric-powered transportations. Despite its mechanical instability upon alloying with Li, nanostructured Si, primarily Si NWs, remains a very interesting material for LIB anodes for several reasons: (a) Si provides the highest known specific capacity for room-temperature electrochemical lithiation (3800 mA h g^{-1}), an order of magnitude higher than that of graphite; (b) Si has low delithiation potential (0.4 V against Li/Li^+), indicating high battery voltages; (c) Si NWs can be directly connected to the current collector without additional binders or conducting additives; (d) high-aspect-ratio Si NWs can prevent fragmentation and offer rapid charge transport and hence cycling rates due to direct 1D electronic pathways [87, 192]. Table 2 presents a summary of the reported high-performance Si NW HS-based LIBs and their performances.

Due to the poor conductivity, Si NW electrodes required a conducting shell, and carbon is proven to be the best overcoating material to increase not only the cycling rate but also the electrode lifetime. A variety of carbon-based materials, such as carbon, graphite, graphene, CNT, RGO etc, have been used to improve the cycling rate, cycling stability, durability and CE of the Si NW-based LIB [119, 120, 180–183, 193, 194]. Using a conductive carbon skin, the Si NW anodes exhibited capacities of over 2000 mA h g^{-1} for 100 cycles when cycled at 0.1 C and over 1200 mA h g^{-1} when cycled more rapidly at 1 C against Li metal. The carbon skin performs a dual role: it speeds lithiation of the Si NWs significantly, while constraining the final volume expansion, which results in recyclability [180]. Multiwalled CNTs as the conducting additive was found to be more effective for obtaining good cycling behavior than using amorphous carbon [183]. Cho *et al* introduced N-doped graphite as the conducting layer on Si NWs [119], which showed higher stability because graphitic layers serve as efficient Li

Table 2. Summary of the reported Si NW HS-based anodes and their LIB performances.

HS system	Capacity in 1st cycle (mA h g^{-1})	Cycles, *n*	Capacity after *n*th cycle (mA h g^{-1})	Reference
Si NWs–a-Si	1060	100	901	[179]
Si NWs–cCarbon	~2500	100	~2000	[180]
	~1200		~1200	
Si NWs–RGO	3350	20	3350	[181]
Si NWs–graphitic	2100	45	1040	[119]
Si NWs–graphene	3924	200	2400	[182]
Si NWs–MWCNT	4250	50	1350	[183]
Si NWs–Cu	2967	30	2138	[184]
Si NWs–Sn	3192	100	1874	[185]
Si NWs–Al	3347	100	1300	[186]
Si NWs–Mg	3209	100	~980	[187]
Si NWs–Au	3362	100	~2000	[188]
Si NWs–TiO_2	3000	100	1600	[189]
Si NWs–TiN	2915	100	1566	[190]
NiSi NWs–a-Si–Al_2O_3	3000	90	3000	[126]
Si NWs–PEDOT	3850	100	2510	[191]

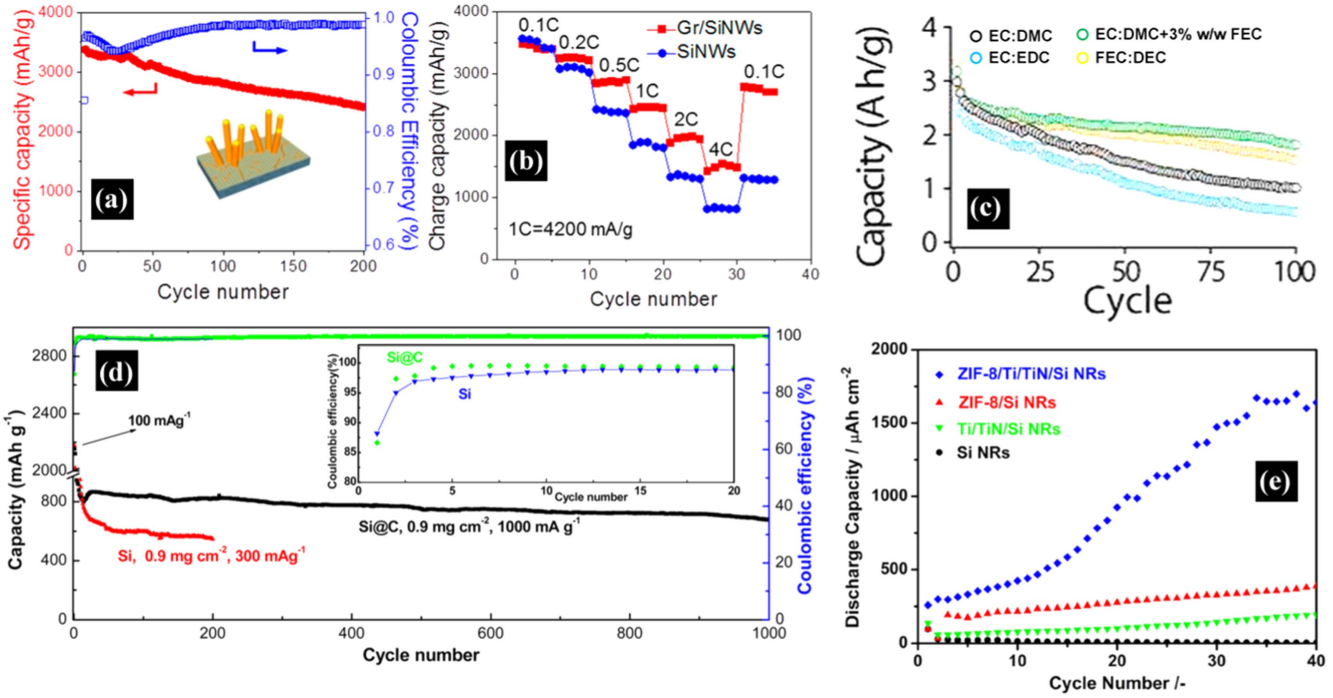

Figure 10. (a) Charge capacities (red circles) and CE (blue squares) of Si NW–graphene anode during 200 cycles at the charging and discharging rate of 0.1 C. (b) Charge capacities of Si NW anode (blue circle) and Si NW–Gr anode (red square) with different cycle rates [182], copyright 2015 American Chemical Society. (c) Discharging capacities of the as-prepared (with Au) Si NW–C anode-based LIB with NaAlg binder using various 1:1 w/w electrolytes [188], copyright 2012 American Chemical Society. (d) Capacity stability of the Si NW–C and Si anodes at loading of 0.9 mg cm^{-2}. The inset shows the corresponding CE [193], copyright 2015 American Chemical Society. (d) Discharge capacities of ZIF-8–TiN–Ti–Si NR electrodes under the current density of 10 μA cm^{-2} within the voltage window from 0.13 to 2.0 V versus Li/Li^+ until the 30th cycles [125], copyright 2016 American Chemical Society.

intercalation sites to protect the Si NW core and it was as effective as the pyridine-like structures for Li storage [119]. With the Si NW–graphene electrode, a charge capacity of 2470 mA h g^{-1} was realized, which was much higher than the 1256 mA h g^{-1} of a porous Si NW–C-black electrode and 6.6 times the theoretical capacity of commercial graphite [194]. Very recently, Xia *et al* showed that graphene acts as an interfacial layer between the current collector and the Si NW anode, and as compared to a Si NW anode on a bare collector the cycling stability of the Si NW/graphene anode was improved by more than 170%, with capacity retentions of ~2400 mA h g^{-1} over 200 cycles [182]. The graphene interface eliminates the formation of parasitic Si films, that undergo severe pulverization and delamination during cycling. In addition, graphene behaves as an excellent diffusion barrier, preventing the interfacial reaction with Li^+ ions

that has a negative effect on the cycling capability [182]. Figure 10(a) shows the capacities and Coulombic efficiencies (CEs) of the Si NW–of graphene anode during 200 cycles at a cycling rate 0.1 C. Figure 10(b) depicts the capacities of the Si NW anode and Si NW–graphene cycled at different rates [182].

Coatings consisting of conducting polymers, such as PEDOT, have also been used to improve the cycling properties of Si NWs [191]. For the first cycle, charge capacities reached 3850 mA h g^{-1}, while the discharge capacities for the second and 100th cycles were 3263 and 2510 mA h g^{-1}, respectively [191]. Si NWs coated with different metal NPs, such as Cu [184], Mg [187], Al [186], Sn [185] and Au [188], acting as anodes in LIBs exhibited high capacity, excellent CE, increased cycle rate and enhanced capacity retention after many cycles. The Cu-coated Si NW electrodes exhibited a high capacity (2700 mA h g^{-1} at first cycle) and good capacity retention with excellent rate capability as compared to the pristine and carbon-coated Si NWs [184].

The formation of a solid electrolyte interphase (SEI) on the surface of the anode due to decomposed electrolyte is a major problem for long life cycle of the battery. A coating consisting of Al_2O_3, TiO_2, TiN etc on Si NWs was used to prevent SEI formation for durable performance [126, 189, 190]. The capacity retention after 100 cycles for the Si NW–TiO_2 HS is twice that of the uncoated Si NWs at 0.1 C, and more than three times higher at 5 C [189]. To preserve the integrity of the whole LIB battery, binders are required, and an appropriate choice of electrolyte plays a crucial role in the prevention of a stable SEI layer [87, 188, 192, 195]. Chockla *et al* showed that a Si NW anode-based LIB with sodium alginate binder and fluoroethylene carbonate electrolyte could perform with best capacities up to 2000 mA h g^{-1} after the first 100 cycles as compared to the other combinations (figure 10(c)). Au decoration on Si NWs yielded a faster cycling rate and a better stability [188]. Carbon-coated Al/Na-doped and defect-abundant Si nanorod-based anodes have shown excellent electrochemical performance with high CE (~99.7% after five cycles) [193]. The HS electrode displays a reversible capacity of about 2200 mA h g^{-1} at 100 mA g^{-1} current, and remains at about 700 mA h g^{-1} over 1000 cycles at 1000 mA g^{-1} with a capacity decay rate of 0.02% due to the formation of an artificial Al_2O_3 SEI prevention layer (as shown in figure 10(d)) [193].

Very recently, metal–organic frameworks (such as ZIF-8) have also been introduced as a stable SEI prevention layer in the case of LIBs [125]. Yu *et al* used ZIF-8–Si NW composite anodes without pyrolysis. However, the capacity was not considerable due to their poor conductivity (specific capacity up to 500 μA h cm^{-2}). With the employment of a conducting buffer layer of TiN–Ti in between the Si NW core and ZIF-8 shell, an enhanced capacity of about 1650 μA h cm^{-2} was realized ((figure 10(e)), with the high CE of about 99% [125]. Overall, there has been tremendous advancement in the application of Si NWs for high-performance LIBs, as succinctly reviewed recently by Kennedy *et al* [196]. However, electrode cracking, pulverization problems related to phase transformations and huge volume expansions (320%) for repeated Li insertion/extraction resulting in the degradation of the Si-based anode etc are the major issues for the commercialization of Si NW HS-based LIBs.

3.7. Supercapacitors

Supercapacitors with high power density, fast charge–discharge kinetics and long cycle life are an attractive energy storage device for various applications. Traditional supercapacitors are mainly carbon-based materials where capacitance and energy density are still relatively low as compared to the batteries. The last few years have witnessed a rapid growth of research on the use of Si NWs as electrode materials for supercapacitors due to their fascinating capacitive properties. In order to improve the performance and achieve synergistic effects, a combination of different inorganic and organic materials with Si NWs has been proposed. In 2010, Chang *et al* reported the fabrication of Si NW-based nanocapacitor arrays using MACE in conjunction with electrodeposition of Ni [197]. The capacitance of the HS device increased by two orders of magnitude over the plate capacitors with the same footprint [197]. Later, the electrochemical properties of supercapacitors based on Si NW HSs with different materials, such as NiO [198], SiC [199], MnO_2 [200], ZnO [201], ZnO/Al_2O_3 [201], carbon [202], PEDOT [203], PEDOT–diamond [204], polypyrrole (PPy) [205] etc, have been studied. An Si NW supercapacitor array with a ZnO and Al_2O_3 bilayer showed an ultrahigh equivalent planar capacitance (EPC) of about 300 μF cm^{-2}, which was 30 times higher than those previously reported for metal–insulator–metal or metal–insulator–semiconductor capacitors [201]. The large EPC value was attributed partly to the large surface area of the densely packed Si NW and partly to the ultrahigh dielectric constant of the nanophase ZnO. Dubal *et al* fabricated a 3D hierarchical assembly of ultrathin MnO_2 nanoflakes on Si NWs for high-performance microsupercapacitors in Li-doped ionic liquid [200]. The high conductivity of the Si NW arrays combined with the large surface area of the ultrathin MnO_2 nanoflakes was responsible for the remarkable performance of the MnO_2@Si NW HS, which exhibited high energy density and excellent cycling stability. The supercapacitor with the HS electrode exhibited highest capacitance of 13 mF cm^{-2} and excellent cycling performance, with 91% retention after 5000 cycles [200]. The Si NW–PEDOT hybrid device exhibited long lifetime and an outstanding electrochemical stability, retaining 80% of the initial capacitance after 1000 cycles at a high current density of 1 mA cm^{-2}. The improvement in the capacitive properties as compared to the bare Si NWs was attributed to the pseudocapacitive behavior induced by the conducting polymer coating [203]. A remarkable cycling stability with a loss of approximately 30% after 10 000 charge–discharge cycles was obtained from a PPy-coated Si NW supercapacitor [205]. Very recently, Devarapalli *et al* reported glucose-derived porous C-coated Si NWs as an efficient electrode for aqueous microsupercapacitors [202]. The capacitance reached 25.64 μF cm^{-2} with a good stability up to 25 000 cycles in 1 M Na_2SO_4

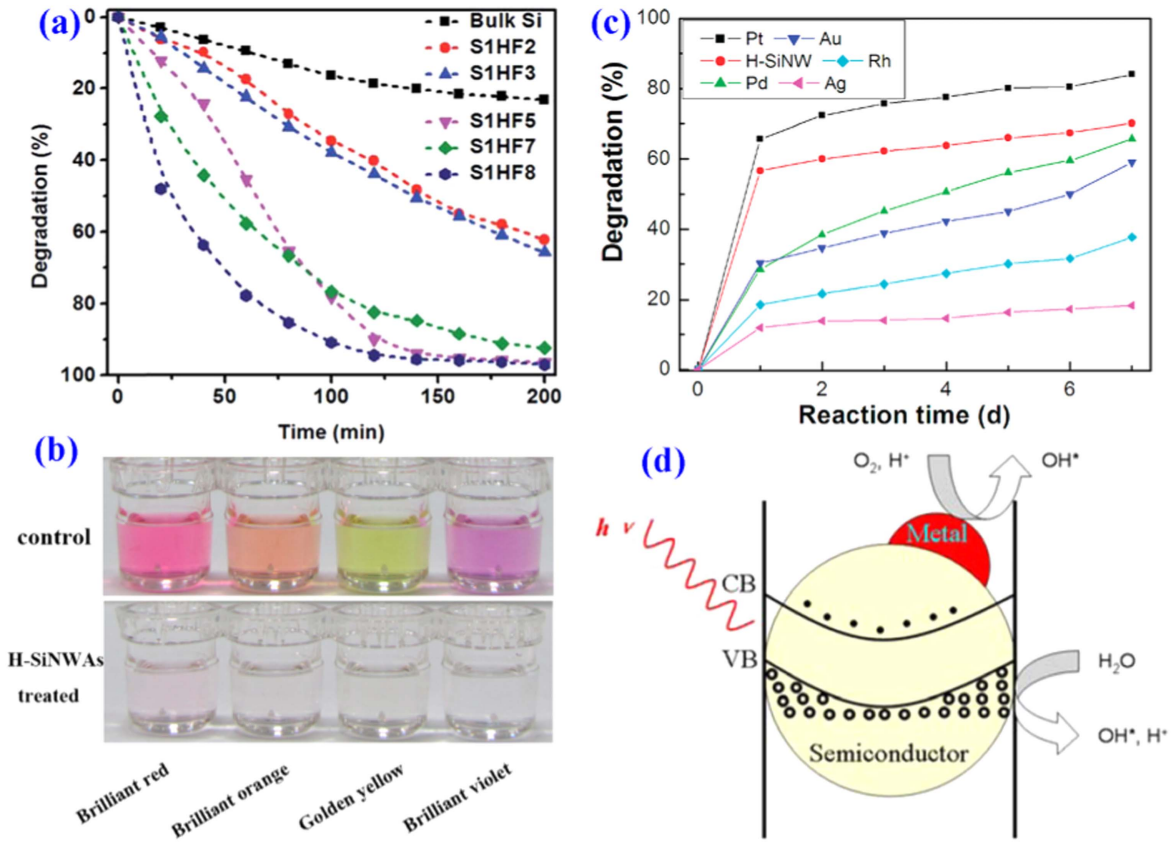

Figure 11. (a) Comparison of the visible-light photodegradation of MB in the presence of MACE-grown Si NWs at various concentrations of HF [103], copyright 2016 Royal Society of Chemistry. (b) Decoloration of different azo dyes in the presence of H–Si NWs [209], copyright 2013 American Chemical Society. (c) Degradation of RhB under various Si NW-based catalysts for different times (days). (d) Schematic diagram of the electron–hole generation in a metal–semiconductor photocatalyst. The mechanisms involved: (left) a ray promotes the formation of the electron and hole, (middle) the electron transfers to the metal and leads to the production of OH^*, (right) the hole is used in the formation of the OH^* groups promoting oxidizing processes [17], copyright 2009 American Chemical Society.

aqueous solution [202]. Despite several advances, the low energy density, lower stability and production cost are the main issues for the commercialization of the Si NW-based supercapacitors as compared to other energy storage devices.

4. Environmental cleaning and monitoring

4.1. Photodegradation of organic dyes

Si NWs are an ecofriendly, photostable, inexpensive and nontoxic material and are able to absorb near UV, visible and NIR light for the degradation of organic pollutants [48, 134, 137, 206]. To overcome the limitations of Si NW-based materials for environmental cleaning, several strategies have been developed in the past, and the most widely used one is photocatalytic heterojunctions incorporating semiconductors, metals and other functional species [17, 48, 134, 206–208]. Si NWs functionalized with –H have shown excellent photocatalysis for the photodegradation of organic pollutants [17, 103, 109, 134]. High-aspect-ratio, Si NC-decorated Si NWs with Si–H-terminated surface grown by MACE have shown excellent photocatalytic nature under visible-light illumination [17, 103, 109, 134]. The variation in HF concentration during the MACE growth of Si NWs creates change in the Si–H-terminated surface and results in the photodegradation of methylene blue (MB). Figure 11(a) shows that the photocatalytic efficiency of Si NWs increases as the HF concentration increases during the growth of Si NWs. H–Si NWs show strong reducing capacity for the reduction of azo dyes and MTT (3-(4, 5-dimethyl-2- thiazol)-2, 5-diphenyl-2H-tetrazolium bromide). In the presence of coenzyme, the reducing capacity of H–Si NWs was enhanced [209]. Figure 11(b) shows the decoloration of various remazol azo dyes including Red F3B, Brilliant Orange 3R, Golden RNL 150% and Brilliant Purple 5R after 3 h in H–Si NW aqueous solution. H–Si NWs were also found to have catalytic activities similar to those of the biological enzymes catalase and peroxidase, and can be used for oxidation of the ligand precursor ophenylenediamine (OPD) [210]. These results suggest that H–Si NWs can be used as enzyme mimics in biotechnology.

Metal NP-decorated Si NW HSs are studied extensively for the photodegradation of organic pollutants, such as MB, methyl red (MR), methyl orange (MO), phenol, Rhodamine 6G (R6G), benzyl alcohol, Rhodamine B (RhB) etc. The main advantages of using noble metals with Si NWs as photocatalysts are (i) the high work function of noble metals (Pt,

Pd, Au, Ag, etc) facilitates the electron transfer from Si NWs to noble metal in the Schottky junction, which significantly reduces the recombination of photogenerated e–h pairs, and (ii) higher absorption due to the SPR effect of noble metals. Shao *et al* studied the photodegradation of RhB by Si NWs modified with Au, Ag, Pd, Pt and Rh NPs and showed that the Pt-modified Si NWs are excellent photocatalysts because they have the highest work function (5.65 eV) [17]. Figure 11(c) shows the degradation of RhB by various metal-modified Si NW catalysts as a function of time, while Figure 11(d) shows a schematic diagram of the e–h generation process in H–Si NWs and metal–semiconductor photocatalyst under light illumination [17]. Megouda *et al* showed that the photocatalytic activity of the H–Si NWs was significantly enhanced after Cu NPs were loaded onto them [134]. Liao *et al* reported that Au–Pd and Pd–Ni bimetal decoration on Si NWs results in a higher degradation rate of p-nitroaniline as compared to the single-metal-decorated Si NWs [206]. Duan *et al* introduced the inert conductive polymer PEDOT in between Ag NPs and Si NWs and found that Si NW–PEDOT–Ag NPs show about 92% photodegradation of RhB, while the H–Si NWs show only about 51% degradation in 180 min [136]. At the same time, Si NW–PEDOT–Ag NPs show excellent stability as compared to the H–Si NWs. Chen *et al* demonstrated a Si NW–TiO_2 microparticle combined photocatalyst, which can respond to both UV and visible light more efficiently than the conventionally used TiO_2 for the degradation of RB5 azo dyes [208]. Si NWs coated with CdSe NPs have shown excellent photodetection and photocatalytic activity for the degradation of MB and acid fuchsin [133]. 3D branched Si NW/NR HSs realized with radial ZnO NWs on the Si NR surface were fabricated by Song *et al*, and it was demonstrated that the branched structures improved the light harvesting ability due to an increased optical path by multi-scattering at its enlarged contact area with the sample solution, and this resulted in high photodegradation of MR [207]. Si NW–TiO_2 core–shell HSs were used as a photocathode in PEC and showed excellent PEC activity in the degradation of phenol under UV or visible–NIR light illumination [79, 80]. The degradation efficiency using a p-Si NW–TiO_2 cathode was 17.7 times higher than that of TiO_2 film on p-type Si wafer. Low reflectance, higher surface area, effective e–h separation and fast interfacial charge transfer were believed to be responsible for this.

4.2. Light-driven CO_2 reduction

The reduction of CO_2 in a PEC cell by solar irradiation is an attractive strategy for environmental cleaning. Besides TiO_2, Si NW HSs are also used as photoelectrodes, and show excellent PEC activity for CO_2 reduction under visible–NIR light illumination. LaTempa *et al* reported the reduction of CO_2 in a saturated aqueous $NaHCO_3$ solution using a p–n junction PEC cell [176]. The p-type Si NWs were used as the photocathode and n-type TiO_2 nanotube films were used as the photoanode. Under bandgap illumination, the PEC cells can convert CO_2 into hydrocarbon fuels, CO and also H_2 due to water splitting. In addition, C3–C4 hydrocarbons, methane and ethylene were formed at the combined rate of 201.5 nM cm^{-2} h^{-1} at an applied potential of −1.5 V versus Ag–AgCl. The reduction rate was enhanced by using a Cu NP-decorated p-Si NW photocathode. Si–H NW photocathodes and Mn-based carbonyl bipyridyl complexes as homogeneous molecular catalyst were used for the reduction of CO_2 to CO in hydroorganic medium [177]. Liu *et al* used a p-Si NW array by mimicking the CO_2 fixation reaction in the Calvin cycle instead of direct reduction of CO_2 by photogenerated carriers [178]. CO_2 was first fixed by the surface-modified benzophenone groups on the Si NWs. A PEC carboxylation reaction was then driven by the photogenerated carriers. This system showed a Faradaic efficiency of over 94% under AM 1.5 illumination at a low overpotential [178]. However, reduction of CO_2 to organic compounds is rather difficult because the reaction involves complex multi-electron reduction processes [15, 176]. Therefore, more sustained efforts are needed to develop efficient photocatalysts that utilize a maximum amount of solar energy to drive significant CO_2 reduction.

4.3. Chemical sensors

Si NWs, possessing excellent charge transport properties and an environment friendly nature, have been demonstrated as excellent candidates for sensing of biochemical molecules. Individual Si NWs as well as their HSs can act as a charge accumulation and depletion site, inducing large change in the electrical properties by the attachment of chemical or biological species. The surface-dependent unique electronic and electrical properties of the Si NWs and their HSs have attracted considerable research attention for the fabrication of NW FETs, and it is found that with appropriate surface passivation the Si NW HSs can significantly improve the performance of FET-based sensors. Among various chemical sensing techniques, Si NW-based FETs were first introduced in 2001 by Cui *et al* and since then have attracted much attention in the semiconductor industry [211]. Si NW FETs modified with calmodulin were used to detect calcium ions (Ca^{2+}), which are important for activating biological processes, such as muscle contraction, protein secretion, cell death and development [211]. High-sensitivity detection of toxic heavy-metal cations such as Cd^{2+} and Hg^{2+} based on a Si NW FET sensor has been demonstrated by Luo *et al* [212]. The Si NW surface was modified with mercaptopropyl silane (MPTES) and the HS FET was capable of detecting Cd^{2+} and Hg^{2+} concentrations as low as 10^{-4} and 10^{-7} M, respectively [212]. Wipf *et al* coated a thin film of Au over Al_2O_3-passivated Si NW FETs for Na^+ sensing via pH response [213]. The authors compared the signal between the Si NWs functionalized with a self-assembled monolayer of thiol-modified crown with the bare Si NWs, since thiol only reacts with (reduced) Au atoms, leaving the number of hydroxyl groups unchanged. Figure 12(a) shows a schematic diagram of the Au-coated Si NW FET for the detection of Na^+. Figure 12(b) shows the differential threshold voltage (ΔV_{th}) of Au-coated NWs (active 15-crown-5-control gold) versus the electrolyte

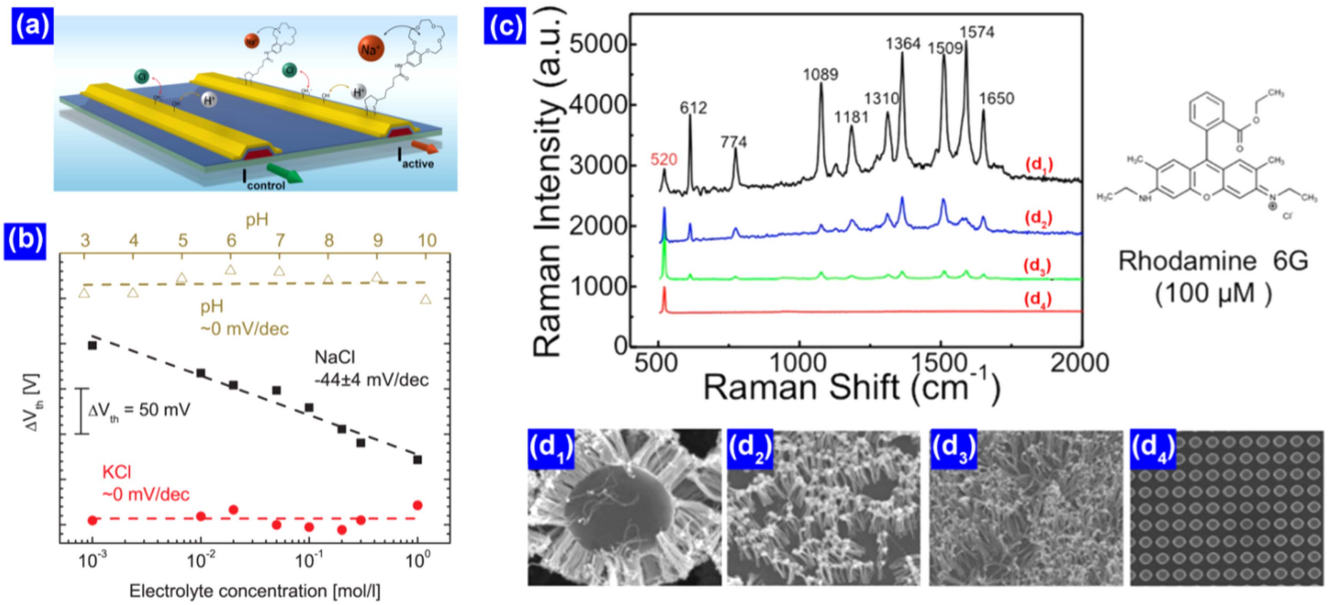

Figure 12. (a) Schematic diagram of Au-coated Si NW FET for the detection of Na^+. The immobilization reaction scheme of the Na-selective crown ether on gold. (b) Differential threshold voltage (ΔV_{th}) of Au-coated NWs (active 15-crown-5-control gold) versus the electrolyte concentration and pH [213], copyright 2013 American Chemical Society. (c) SERS spectra of R6G obtained from Au nanostructures. (d_1)–(d_4) Corresponding SEM images, respectively [131], copyright 2015 American Chemical Society.

concentration and the pH. The crown ether shows a high selectivity toward the Na^+ [213].

Optical-based surface-enhanced Raman scattering (SERS) by metal NP-decorated Si NW HSs is another efficient way of sensing chemical and biological molecules with surface-seeking groups, since only molecules on or near the metal surface experience the large near-field enhancements upon resonant plasmon excitation. Si NWs coated with metal NPs, mainly Ag, Au, Pd, Cu and Pt, have been used as SERS effective substrates for sensing a variety of inorganic and organic molecules, such as 4-methylbenzenethiol [46], crystal violet [25, 214, 215], RhB [216], R6G [16, 25, 131, 214, 215], MO [214], nicotine [25], carbaryl [215], calcium dipicolinate [217] (CaDPA), p-aminothiophenol [214] (PATP), 4-aminothiophenol [218] etc. Shao *et al* showed that SERS effective Ag NP-decorated Si NWs could detect R6G (1×10^{-16} M), CV (1×10^{-16} M) and nicotine (1×10^{-14} M) very efficiently [25]. Han *et al* fabricated highly sensitive, reproducible and stable SERS sensors based on well controlled Ag NP-decorated Si NWs as building blocks and utilized them for the detection of a low concentration of carbaryl (0.01 mg ml^{-1}) residues on a cucumber surface with 1 s acquisition time [215]. Huang *et al* synthesized Au NW bundles, which were grown radially outward from Si NWs, as a SERS effective substrate for probing R6G (figure 12(c)) [131]. The authors studied the SERS signals from four representative samples: (i) Au NWs on an Si pillar umbrella structure (figure 12(d_1)), (ii) Au NW bundles (figure 12(d_2)), (iii) loose Au NWs (figure 12(d_3)) and (iv) as-prepared Si pillars without any Au structure (figure 12(d_4)). Undoubtedly, SERS signal intensities for case (i) showed the largest enhancement as compared to the other samples, with an R6G detection limit of 10 μM [131]. Si NW–metal NP-based surface-enhanced fluorescence spectra are also used to detect some lanthanide ions, such as Pr^{3+}, Nd^{3+}, Ho^{3+} and Er^{3+} [219]. Wang *et al* fabricated a fluorescence sensor with a naphthalimide derivative on the surface of Si NWs for H_2S detection [220].

4.4. Biomolecular sensors for microbial monitoring

In recent years, there has been enormous activity in the development of functionalized Si NW FET-based biosensors for applications in toxin testing, biomolecule detection, medical diagnosis, food purity detection, environmental monitoring and many other areas of biochemical industry [211, 221, 222]. Rim *et al* reviewed biosensitive FETs based on Si NWs passivated with different passivating layers for nucleic acid detection, immunological detection, cell signal detection and the kinetics of biological species [223]. Cui *et al* fabricated biotin-modified Si NW-based FETs for selective detection of biological and chemical species [211]. Biotin-modified Si NWs were used to detect streptavidin down to a picomolar concentration range. In addition, antigen-functionalized Si NWs showed reversible antibody binding and concentration-dependent detection in real time. A sensitivity down to a concentration of 10 pM was demonstrated for the detection of streptavidin by the biotin-modified Si NWs [211]. Chen *et al* fabricated a Si NW HS FET modified by magnetic graphene with long-chain acid groups (MGLA) to detect apolipoprotein A II protein (APOA2 protein), a biomarker for the diagnosis of bladder cancer [224]. Modified with different organic biomolecules, Si NW HS-based FETs were used for the detection of nucleic acids, proteins, protein–DNA interactions, small molecule–protein interactions, cells and viruses and diagnosis of different kinds of disease such as dengue, cancer etc [221, 222, 225, 226].

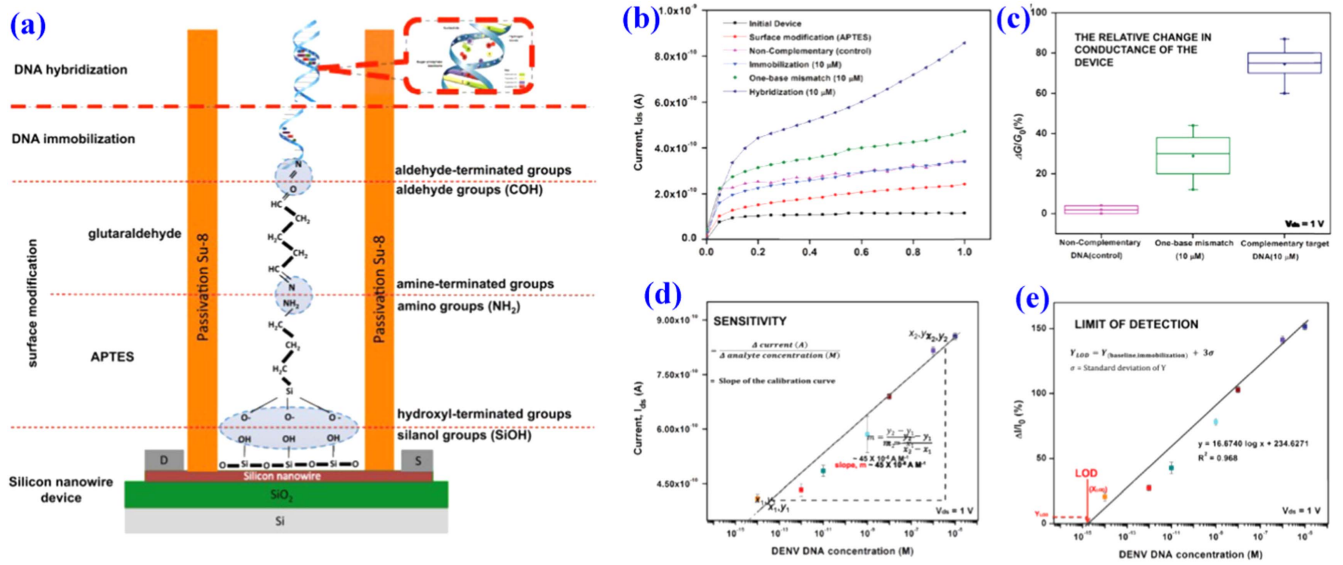

Figure 13. (a) Schematic illustration of the detection of DENV DNA. (b) I_{ds}–V_{ds} characteristic for different steps of surface functionalization. (c) Hybridization specificity demonstrated by the conductance to the complementary, one-base-mismatched and non-complementary DNA sequences at $V_{ds} = 1$ V. (d) I_{ds} response curve of Si NW biosensor with different concentrations of DENV DNA. (e) Calibration curve of the relative change in current, display limit of detection [225], copyright 2016 Elsevier.

Adam *et al* fabricated an APTES-modified Si NW (amine-terminated surface)-based highly sensitive biosensor with novel liquid gate control technology for the detection of specific single-stranded DNA molecules [226]. The sensor selectively detects the target ssDNA, with a linear response to concentration from 100 pM to 25 nM. A high sensitivity (>95%) was achieved even after 1000 cycles, confirming the reliability of the device [226]. Very recently, Nuzaihan *et al* reported a multi-functionalized Si NW FET with appropriate molecular gate for the detection of dengue virus (DENV), and it was able to detect as low as 2.0 fM concentration at a greatly enhanced sensitivity of 45.0 μA M^{-1} with high specificity, repeatability and reproducibility [225]. A typical detection process is shown schematically in figure 13(a), and consists of three steps: functionalization of the Si NWs, DNA immobilization and DNA hybridization. Figure 13(b) depicts the *I*–*V* characteristic, that exhibits significant differences in the measured I_{ds} values for each of the DNA hybridizations. It was observed that upon hybridization with a fully complementary target DNA and one-base-mismatched target DNA, increases in current of 0.52 nA and 0.13 nA were recorded, respectively. Significant change (74%) in the conductance was observed for the fully complementary target DNA, while the conductance changes between one-base-mismatched target DNA and the immobilized DNA probe resulted in a smaller increase in conductance (28%) (figure 13(c)). The sensitivity (45.0 μA M^{-1}) and limit of detection (2 fM) were extremely good as compared to the previous reports in the detection of DENV DNA, as shown in figures 13(d) and (e) [225]. One of the major issues in using a Si NW FET for a biosensor is its mechanical stability. Suspended Si NWs with high aspect ratio can buckle or break. This problem has been overcome by using a honeycomb Si NW structure [227]. The honeycomb Si NW device exhibited excellent electrical characteristics, such as lower subthreshold swing, higher transconductance, higher linear drain current, higher mechanical stability and better pH sensitivity as compared to the suspended Si NW-based devices [227].

SERS effective Si NW HSs have been exploited for sensing a variety of biomolecules, such as DNA [25, 228], immune reagents [229] and bacteria [215, 217] (*E. coli*, *Bacillus anthracis*) etc. Shao *et al* showed that SERS effective Ag NP-decorated Si NWs could detect calf thymus DNA (1×10^{-8} mg ml^{-1}) very efficiently [25]. Han *et al* used the SERS effective Si NW–Ag HS sensor on a commercially available filter film for label-free, real-time detection of *E. coli* in drinking water [215]. Si NW–metal NP HS SERS substrate is also used for the label-free immunoassay detection [229]. A Ag NP-coated Si NW array exhibited strong SERS spectra of mouse immunoglobulin G (mIgG), goat–anti-mouse immunoglobulin G (gamIgG) and immune complexes formed from 4 ng each of mIgG and gamIgG [229]. The enhancement of Raman signal was explained by two kinds of plasmon resonance: local resonance from each individual Ag NP and a surface electromagnetic wave on the whole Si NW–Ag substrate surface [229]. Akin *et al* showed that metal NP-coated Si NWs could be a better SERS effective substrate after surface modification by polydopamine [230]. Si NW HSs are also used to detect biomolecules such as proteins and DNA using florescence detection [231, 232]. Su *et al* recently developed a novel Au NP-decorated Si NW-based molecular beacon for high-sensitivity multiplex DNA detection [231], while Han *et al* used APTES-modified Si NWs for an immunosensor using fluorescence detection of protein [232]. Thus, there is a huge potential for the application of Si NW HSs in health care and life sciences, though commercialization of the devices remains a considerable challenge.

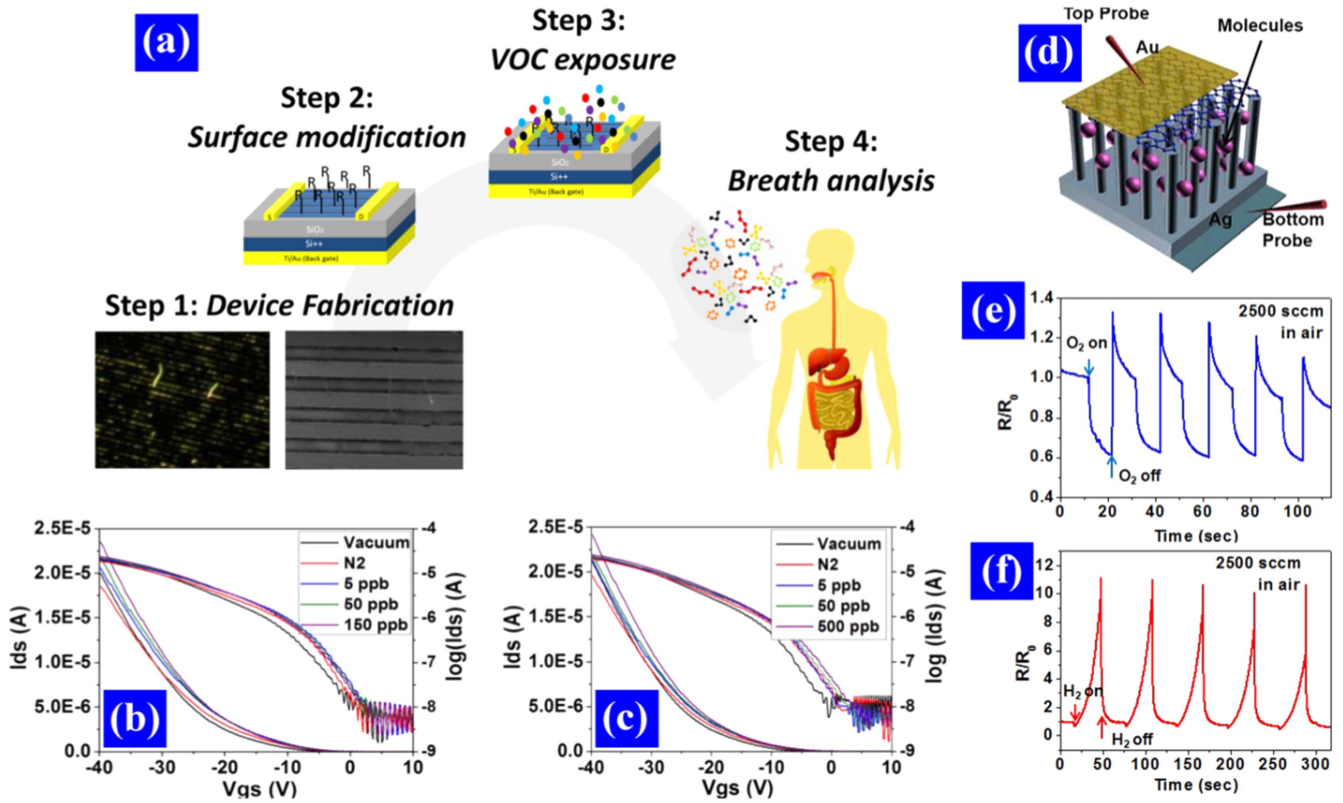

Figure 14. (a) Schematic diagrams of device fabrication and testing of Si NW FET-based gas sensor. (b), (c) Representative examples of I_{ds}–V_{gs} curves of TPS in vacuum, upon exposure to N_2 and upon exposure to increasing concentrations of 6-methyl-5-hepten-2-one (b) and nonanol (c) [239], copyright 2015 American Chemical Society. (d) Schematic illustration of Si NW–graphene sensor. (e), (f) Normalized resistance responses of the fabricated gas sensor under repeated exposures of O_2 (e) and H_2 (f) gases in air at RT [39], copyright 2014 Nature Publishing Group.

4.5. Gas sensors

The sensitive and selective detection of toxic and harmful gases is of paramount importance for keeping the environment safe. Si NW HSs have been exploited in gas-sensing applications for the detection of different hazardous and nonhazardous gases. Compared to the conventional sensors based on flat Si films, the NW gas sensors exhibit many impressive characteristics, such as ultrahigh sensitivity, fast response time, higher selectivity, low power consumption and better stability. Due to the small gaps in the NW array with high aspect ratio, a few gas molecules are sufficient to change the electrical properties of the sensing elements. This allows the detection of a very low concentration of gas within a few seconds. H_2 [39, 233, 234], H_2S [233], NH_3 [233, 235], CO [233], O_2 [39, 233, 234], NO [233], NO_2 [233, 236], humidity [237], TNT [238], acetic acid [235], different VOCs (hexane, octane, decane, hexanol, ethanol, octanol, decanol) [141], volatile linkers used in medicine [239] etc have been successfully detected with high accuracy and sensitivity by Si NWs heterostructured with different materials.

Si NW-based chemical FETs (CHEM-FETs) have been widely used to sense gases for both reducing gases or electron donors (e.g., H_2, H_2S, NH_3, CO) and oxidizing gases or electron acceptors (e.g., O_2, NO, and NO_2) [233]. Han *et al* demonstrated a Si NW–SnO_2 HS-based chemically gated FET (CGFET) using Si NW as the current conducting channel and a 2D SnO_2 thin film on top of the Si NWs as the gas sensitive material for selective sensing of different oxidizing and reducing gases [233]. The sensor response and sensitivity are much improved as compared to conventional devices, such as chemiresistor-based FETs [233]. Through the peptide sequence, the Si NW–peptide sensor exhibited orthogonal responses to acetic acid and ammonia vapors. The sensing selectivity arises from both acid–base reactivity and from molecular structure [235]. Si NWs coated with self-assembled monolayers of APTES, which were further functionalized with $-CH_3$, $-C_6H_5$, $-COOH$ and $-COOCH_3$, have been used for the detection of various VOCs in gas phase [141]. Wang *et al* reported that Si NW FETs coated with alkane–silanes, aldehyde–silanes or aminosilanes give different responses and sensitivities when exposed to hexane at 1000 ppm [141]. Shehada *et al* fabricated a gas sensor based on Si NW FETs coated with trichloro-(phenethyl)silane (TPS), which have high detection limit down to 5 ppb, for the selective detection of VOCs that are linked with gastric cancer conditions in exhaled breath [239]. Figure 14(a) shows a schematic illustration of the steps involved in the fabrication of the gas sensor. Figure 14(b) presents the I_{ds} versus back-gate voltage (V_{gs}) curves of TPS on exposure to 6-methyl-5-hepten-2-one, while figure 14(c) shows the same for nonanol. These results indicated that TPS was selective for nonanol

(one of the biomarkers of gastric cancer from exhaled breath), but not for 6-methyl-5-hepten-2-one (one of the confounding environmental VOCs that does not relate to gastric cancer) in this range of concentrations [239].

Noh *et al* fabricated Pd-coated Si NW-based sensors for H_2 and O_2 sensing [234]. The Pd-coated rough Si NWs showed good reversibility and excellent H_2 sensing performance in terms of sensitivity (>300%), response time (<3 s) and detection limit (~5 ppm) [234]. Kim *et al* fabricated a Si NW–graphene HS molecular gas sensor [39].

Figure 14(d) shows a schematic illustration of the Si NW–graphene sensor and the configuration of the HS used for the characterization. The HS device showed a highly rectifying property with an 'on/off' current ratio of about $\sim 10^2$ at ±5 V, indicating well defined behavior of Schottky diodes. Figures 14(e) and (f) show the electrical responses of the Si NW–graphene diode as a molecular sensor to periodic switches of O_2 and H_2 exposures with intervals of 10 and 30 s at a flow rate of 2500 sccm, respectively, in air at room temperature. The HS sensor shows high sensitivity of 1280% resistance changes under H_2 exposure, whereas 37% under O_2 exposure [39]. Thus, the selectivity was quite good for the NW HS. Ma *et al* fabricated Si NW–WO_3 HS sensors [240] and Liao *et al* fabricated Si NW–ZnO branched HSs [236] for NO_2 sensing. A maximum response of 35.1% resistance change to NO_2 with a concentration of 50 ppm was observed with a detection limit of 5 ppm. The improved sensing behavior was explained by the energy band bending at the heterojunctions between ZnO and Si NWs, faster carrier transportation and more oxygen vacancies when exposed to oxidizing gases [236]. The sensitivity, selectivity of the target material, speed of response and stability of the sensor device are important issues in the field of sensor development in general. Response times of the reported devices are typically at the time scale of seconds to minutes. However, faster response times are needed for demanding applications. Furthermore, the degradation of the selector layer (functionalities) may deteriorate the sensor performance under harsh environmental conditions.

5. Conclusions and outlook

Herein, we have discussed several attractive properties of Si NW HSs and their applications in emerging areas of energy and the environment. The performance of the Si NW HS-based devices strongly depends on the morphology, structure and surface/interface properties of the Si NWs as well as their HSs. We have reviewed the recent research progress in the large-area, low-cost and environment friendly fabrication of Si NWs and Si NW-based HSs for the ensuing applications related to energy conversion, storage, and environmental cleaning and monitoring. In contrast to bottom-up approaches, that have mostly been exploited for fundamental studies, top-down processes are more commonly implemented for the fabrication of ordered arrays of Si NWs of controlled morphology and tunable properties for the wafer-scale fabrication of devices. Si NW HSs of different categories were discussed with their growth strategies, enhanced properties and promising applications associated with each type of HS. The advantage of the HS devices over the conventional Si NW-based devices has been elucidated, with particular emphasis on the improved performance and the stability of the devices. Many researchers are quite affirmative about the real life applications of the Si NW-based HS devices with superior performances, since the properties are being improved continuously through the newer findings. The problems and challenges of utilizing the Si NW HSs and the key parameters to improve the devices' performances are extensively discussed in this review. More intense research on this topic could find the answers to unresolved issues such as high performance, biocompatibility, reproducibility, robustness, stability and low-cost integration of the devices. The future directions will be dependent on a few important steps, such as the following. (1) Improved and novel fabrication processes of Si NW HSs to better control the dimensions, compositions, structures, interfaces, uniformity and yield of the HSs. The development in modern characterization techniques for studying individual Si NWs and their HSs, their ensembles, the nature of interfacial regions and phase boundaries must go down to the atomic level. *In situ* characterization tools need to be employed to address some of these issues. Future device applications of HS materials will require not only improved geometric structures, size distribution and shape uniformity but also large-area alignment, since the properties of nanomaterials are dependent not only on their sizes and shapes but also on their arrangement over macroscopic areas. (2) Although the HSs are superior for modulation of the device properties, the synergistic ('1 + 1 > 2') performance lies in selection of the right materials. Not only inorganic and organic semiconductors or metals, but also different materials such as polymers, ion-coordinating supramolecules, metal–organic charge-transfer complexes, biomolecules etc, are attractive in fabrication of Si NW HSs, which can be utilized to address the future energy crisis and environmental complications. (3) The HS properties and device performance depend on the external parameters of the devices and their mutual interaction with the HS material. For example, in the case of the LIB, the electrolytes and binders greatly influence the electrochemical performances of Si NW HS-based anode materials, as reported recently. The commonly used $LiPF_6$ electrolyte decomposes gradually and produces HF, which can etch a Si NW-based anode. As a result, the LIB exhibits a large irreversible capacity loss (i.e. low Coulombic efficiency) and short cycle life, which encourage scientists to search for more suitable electrolytes and binders to assemble the next generation LIBs with high energy densities and long life cycle. (4) The size of the fabricated device will be a great challenge for the implementation of the device into the real world. For example, in the case of a solar cell, different passivation layers as well as complicated materials with different shapes and sizes are used to overcome the limitations of the fabricated Si NW-based solar cells. In doing so, the overall size of the solar call increases and applicable power cannot be generated from a small device, which prevents the implementation of the solar cells in small

gadgets, such as electronic toys, mobiles, watches and medical electronics. (5) The choice of a suitable flexible substrate without affecting the properties of the HS device will also need significant attention for the implementation of the device into flexible electronics, including flexible light source, flexible sensors etc (6). Efforts should focus also on the application of Si NW HSs as an unusual but highly abundant source of energy: for example, artificial photosynthesis by means of solar water splitting for H_2 generation; photocatalytic conversion of carbon dioxide to fuels. Analogous to the natural photosynthesis process in plants, sunlight absorption, photoinduced charge separation and chemical reactions have to be carefully designed at a microscopic scale to achieved higher efficiency in artificial photosynthesis. (7) More intense research on Si NW HSs for development of the emerging applications, e.g. photodetectors, gene delivery, drug delivery etc, is envisaged. (8) Cost reduction is one of the major future objectives. The economic constraints together with the simple, stable and reproducible device based on Si NW HSs have provided motivation worldwide to explore new strategies that could meet the demands for cost effective energy devices today and in the future.

The choice of appropriate materials for the HSs, control of external layer quality, formation of a high-quality interface between the external material and the NW, reproducibility, biocompatibility, robustness and ability to sustain high lifetime are the challenging issues. It is believed that the above discussion on the growth strategies and novel energy and environmental applications of Si NW HSs will stimulate more intense research in this area for a viable commercialization of some of the devices in the near future.

Acknowledgments

We acknowledge the financial support from CSIR (grant No. 03(1270)/13/EMR-II), DEITY (grant No. 5(9)/2012-NANO (VOL-II)) and BRNS (grant No. 2012/37P/1/BRNS). We would like to thank Dr M Meyyappan, USA, for his valuable suggestions on the manuscript.

References

[1] Bandaru P R and Pichanusakorn P 2010 *Semicond. Sci. Technol.* **25** 024003
[2] Otto M *et al* 2015 *Adv. Opt. Mater.* **3** 147
[3] Hasan M, Huq M F and Mahmood Z H 2013 *SpringerPlus* **2** 151
[4] Liu X, Coxon P R, Peters M, Hoex B, Cole J M and Fray D J 2014 *Energy Environ. Sci.* **7** 3223
[5] Han H, Huang Z and Lee W 2014 *Nano Today* **9** 271
[6] Song T, Lee S-T and Sun B 2012 *Nano Energy* **1** 654
[7] Qu Y, Zhoua H and Duan X 2011 *Nanoscale* **3** 4060
[8] Peng K-Q and Lee S-T 2011 *Adv. Mater.* **23** 198
[9] Huang Z, Geyer N, Werner P, de Boor J and Gosele U 2011 *Adv. Mater.* **23** 285
[10] Shao M, Ma D D D and Lee S-T 2010 *Eur. J. Inorg. Chem.* **2010** 4264
[11] Schmidt V, Wittemann J V and Gösele U 2010 *Chem. Rev.* **110** 361
[12] Schmidt V, Wittemann J V, Senz S and Gösele U 2009 *Adv. Mater.* **21** 2681
[13] Dussart R, Tillocher T, Lefaucheux P and Boufnichel M 2014 *J. Phys. D: Appl. Phys.* **47** 123001
[14] Ramanujam J, Shiri D and Verma A 2011 *Mater. Exp.* **1** 105
[15] Peng K-Q, Wang X, Li L, Hu Y and Lee S-T 2013 *Nano Today* **8** 75
[16] Galopin E, Barbillat J, Coffinier Y, Szunerits S, Patriarche G and Boukherroub R 2009 *ACS Appl. Mater. Interfaces* **1** 1396
[17] Shao M, Cheng L, Zhang X, Ma D D D and Lee S T 2009 *J. Am. Chem. Soc.* **131** 17738
[18] Schubert L, Werner P, Zakharov N D, Gerth G, Kolb F M, Long L, Gösele U and Tan T Y 2004 *Appl. Phys. Lett.* **84** 4968
[19] Choi D-G, Yu H K, Jang S G and Yang S-M 2004 *J. Am. Chem. Soc.* **126** 7019
[20] Morales A M and Lieber C M 1998 *Science* **279** 208
[21] Wu Y and Yang P 2001 *J. Am. Chem. Soc.* **123** 3165
[22] Ghosh R, Giri P K, Imakita K and Fujii M 2014 *Nanotechnology* **25** 045703
[23] Li X and Bohn P W 2000 *Appl. Phys. Lett.* **77** 2572
[24] Peng K Q, Yan Y J, Gao S P and Zhu J 2002 *Adv. Mater.* **14** 1164
[25] Shao M-W, Zhang M-L, Wong N-B, Ma D D-d, Wang H, Chen W and Lee S-T 2008 *Appl. Phys. Lett.* **93** 233118
[26] Kim J, Han H, Kim Y H, Choi S H, Kim J C and Lee W 2011 *ACS Nano* **5** 3222
[27] Kayes B M, Filler M A, Putnam M C, Kelzenberg M D, Lewis N S and Atwater H A 2007 *Appl. Phys. Lett.* **91** 103110
[28] Dasgupta N P, Sun J, Liu C, Brittman S, Andrews S C, Lim J, Gao H, Yan R and Yang P 2014 *Adv. Mater.* **26** 2137
[29] Alferov Z I 2001 *Rev. Mod. Phys.* **73** 767
[30] Chao Z, Zhi X, Wei T, Dai-Ming T, Xi W, Yoshio B, Naoki F and Dmitri G 2015 *Nanotechnology* **26** 154001
[31] Liu H, She G, Huang X, Qi X, Mu L, Meng X and Shi W 2013 *J. Phys. Chem.* C **117** 2377
[32] Prucnal S *et al* 2014 *Nano Res.* **7** 1769
[33] Hocevar M, Immink G, Verheijen M, Akopian N, Zwiller V, Kouwenhoven L and Bakkers E 2012 *Nature Commun.* **3** 1266
[34] Mullane E, Geaney H and Ryan K M 2015 *Phys. Chem. Chem. Phys.* **17** 6919
[35] Chou Y-C, Wen C-Y, Reuter M C, Su D, Stach E A and Ross F M 2012 *ACS Nano* **6** 6407
[36] Amato M, Palummo M, Rurali R and Ossicini S 2014 *Chem. Rev.* **114** 1371
[37] Geaney H, Mullane E, Ramasse Q M and Ryan K M 2013 *Nano Lett.* **13** 1675
[38] Chen L, Fung W Y and Lu W 2013 *Nano Lett.* **13** 5521
[39] Kim J, Oh S D, Kim J H, Shin D H, Kim S and Choi S-H 2014 *Sci. Rep.* **4** 5384
[40] Hu J, Bando Y, Liu Z, Sekiguchi T, Golberg D and Zhan J 2003 *J. Am. Chem. Soc.* **125** 11306
[41] Zhang Y F, You L P, Shan X D, Wei X L, Huo H B, Xu W J and Dai L 2007 *J. Phys. Chem.* C **111** 14343
[42] Hu J, Chen Z, Sun Y, Jiang H, Wang N and Zou R 2009 *J. Mater. Chem.* **19** 7011
[43] Xie C *et al* 2014 *ACS Nano* **8** 4015
[44] Peng K-Q, Wang X, Wu X-L and Lee S-T 2009 *Nano Lett.* **9** 3704
[45] Fang C, Agarwal A, Widjaja E, Garland M V, Wong S M, Linn L, Khalid N M, Salim S M and Balasubramanian N 2009 *Chem. Mater.* **21** 3542
[46] Yang J, Li J B, Gong Q H, Teng J H and Hong M H 2014 *Nanotechnology* **25** 465707

[47] Convertino A, Cuscunà M, Martelli F, Manera M G and Rella R 2014 *J. Phys. Chem.* C **118** 685
[48] Brahiti N, Hadjersi T, Menari H, Amirouche S and El Kechai O 2015 *Mater. Res. Bull.* **62** 30
[49] Sudhagar P, Song T, Lee D H, Mora-Seró I, Bisquert J, Laudenslager M, Sigmund W M, Park W I, Paik U and Kang Y S 2011 *J. Phys. Chem. Lett.* **2** 1984
[50] Shi J, Hara Y, Sun C, Anderson M A and Wang X 2011 *Nano Lett.* **11** 3413
[51] Kargar A, Sun K, Jing Y, Choi C, Jeong H, Jung G Y, Jin S and Wang D 2013 *ACS Nano* **7** 9407
[52] Hwang Y J, Wu C H, Hahn C, Jeong H E and Yang P 2012 *Nano Lett.* **12** 1678
[53] Liu C, Tang J, Chen H M, Liu B and Yang P 2013 *Nano Lett.* **13** 2989
[54] Shi J and Wang X 2012 *Energy Environ. Sci.* **5** 7918
[55] Noh S Y, Sun K, Choi C, Niu M, Yang M, Xu K, Jin S and Wang D 2013 *Nano Energy* **2** 351
[56] Jianga X, Tiana B, Xianga J, Qiana F, Zhenga G, Wang H, Maia L and Liebera C M 2011 *Proc. Natl Acad. Sci. USA* **108** 12212
[57] Wang D, Qian F, Yang C, Zhong Z and Lieber C M 2004 *Nano Lett.* **4** 871
[58] Hu J, Bando Y, Zhan J, Yuan X, Sekiguchi T and Golberg D 2005 *Adv. Mater.* **17** 971
[59] Lv S, Li Z, Chen C, Liao J, Wang G, Li M and Miao W 2015 *ACS Appl. Mater. Interfaces* **7** 13564
[60] Chong S K, Lim E L, Yap C C, Chiu W S, Dee C F and Rahman S A 2014 *Sci. Adv. Mater.* **6** 782
[61] Kargar A, Sun K, Kim S J, Lu D, Jing Y, Liu Z, Pan X and Wang D 2013 *Phys. Status Solidi* A **210** 2561
[62] Putnam M C, Boettcher S W, Kelzenberg M D, Turner-Evans D B, Spurgeon J M, Warren E L, Briggs R M, Lewis N S and Atwater H A 2010 *Energy Environ. Sci.* **3** 1037
[63] Tian B, Zheng X, Kempa T J, Fang Y, Yu N, Yu G, Huang J and Lieber C M 2007 *Nature* **449** 885
[64] Garnett E and Yang P 2010 *Nano Lett.* **10** 1082
[65] Katiyar A K, Sinha A K, Manna S and Ray S K 2014 *ACS Appl. Mater. Interfaces* **6** 15007
[66] Pan L, Lew K-K, Redwing J M and Dickey E C 2005 *Nano Lett.* **5** 1081
[67] Ben-Ishai M and Patolsky F 2010 *Adv. Mater.* **22** 902
[68] Manna S, Das S, Mondal S P, Singha R and Ray S K 2012 *J. Phys. Chem.* C **116** 7126
[69] Yu P *et al* 2013 *ACS Nano* **7** 10780
[70] Zhang F, Han X, Lee S-T and Sun B 2012 *J. Mater. Chem.* **22** 5362
[71] Cheng Y, Fang G, Li C, Yuan L, Ai L, Chen B, Zhao X, Chen Z, Bai W and Zhan C 2007 *J. Appl. Phys.* **102** 083516
[72] Hwang Y J, Boukai A and Yang P 2009 *Nano Lett.* **9** 410
[73] Sun L, He H, Liu C, Lu Y and Ye Z 2011 *Cryst. Eng. Commun.* **13** 2439
[74] Ghosh R, Giri P K, Imakita K and Fujii M 2015 *J. Alloys Compd.* **638** 419
[75] Zhou H, Fang G, Yuan L, Wang C, Yang X, Huang H, Zhou C and Zhao X 2009 *Appl. Phys. Lett.* **94** 013503
[76] Kang H, Park J, Choi T, Jung H, Lee K H, Im S and Kim H 2012 *Appl. Phys. Lett.* **100** 041117
[77] Um H-D, Moiz S A, Park K-T, Jung J-Y, Jee S-W, Ahn C H, Kim D C, Cho H K, Kim D-W and Lee J-H 2011 *Appl. Phys. Lett.* **98** 033102
[78] Kale V S, Prabhakar R R, Pramana S S, Rao M, Sow C-H, Jinesh K B and Mhaisalkar S G 2012 *Phys. Chem. Chem. Phys.* **14** 4614
[79] Yu H, Chen S, Quan X, Zhao H and Zhang Y 2009 *Appl. Catal.* B **90** 242
[80] Yu H, Li X, Quan X, Chen S and Zhang Y 2009 *Environ. Sci. Technol.* **43** 7849
[81] Yenchalwar S G, Azhagan V K and Shelke M V 2014 *Phys. Chem. Chem. Phys.* **16** 17786
[82] Mayer M T, Du C and Wang D 2012 *J. Am. Chem. Soc.* **134** 12406
[83] Li Q and Wang C 2003 *J. Am. Chem. Soc.* **125** 9892
[84] Wang F, Jiang Y, Li T, Zhao Y and Zhang X 2015 *J. Mater. Chem.* A **3** 22902
[85] Subramani T, Syu H-J, Liu C-T, Hsueh C-C, Yang S-T and Lin C-F 2016 *ACS Appl. Mater. Interfaces* **8** 2406
[86] Adachi M M, Anantram M P and Karim K S 2013 *Sci. Rep.* **3** 1546
[87] Zamfir M R, Nguyen H T, Moyen E, Lee Y H and Pribat D 2013 *J. Mater. Chem.* A **1** 9566
[88] Wang N, Zhang Y F, Tang Y H, Lee C S and Lee S T 1998 *Appl. Phys. Lett.* **73** 3902
[89] Dhara S and Giri P K 2011 *Int. J. Nanosci.* **10** 13
[90] Fu Y Q, Colli A, Fasoli A, Luo J K, Flewitt A J, Ferrari A C and Milne W I 2009 *J. Vac. Sci. Technol.* B **27** 1520
[91] Pan H, Lim S, Poh C, Sun H, Wu X, Feng Y and Lin J 2005 *Nanotechnology* **16** 417
[92] Lim K W, Lee J-I, Yang J, Kim Y-K, Jeong H Y, Park S and Shin H S 2014 *ACS Appl. Mater. Interfaces* **6** 6340
[93] Shi W S, Peng H Y, Zheng Y F, Wang N, Shang N G, Pan Z W, Lee C S and Lee S T 2000 *Adv. Mater.* **12** 1343
[94] Liu J L, Cai S J, Jin G L, Thomas S G and Wang K L 1999 *J. Cryst. Growth* **200** 106
[95] Bauer J, Fleischer F, Breitenstein O, Schubert L, Werner P, Gösele U and Zacharias M 2007 *Appl. Phys. Lett.* **90** 012105
[96] Fuhrmann B, Leipner H S, Höche H-R, Schubert L, Werner P and Gösele U 2005 *Nano Lett.* **5** 2524
[97] Jansen H, Boer M d, Legtenberg R and Elwenspoek M 1995 *J. Micromech. Microeng.* **5** 115
[98] Hsu C-M, Connor S T, Tang M X and Cui Y 2008 *Appl. Phys. Lett.* **93** 133109
[99] Pal A, Ghosh R and Giri P K 2015 *Appl. Phys. Lett.* **107** 072104
[100] Bachtouli N, Aouida S and Bessais B 2014 *Microporous Mesoporous Mater.* **187** 82
[101] Peng K, Zhang M, Lu A, Wong N-B, Zhang R and Lee S-T 2007 *Appl. Phys. Lett.* **90** 163123
[102] Hildreth O J, Lin W and Wong C P 2009 *ACS Nano* **3** 4033
[103] Ghosh R and Giri P K 2016 *RSC Adv.* **6** 35365
[104] Li X 2012 *Curr. Opin. Solid State Mater. Sci.* **16** 71
[105] Chen C-Y and Liu Y-R 2014 *Phys. Chem. Chem. Phys.* **16** 26711
[106] Chern W, Hsu K, Chun I S, Azeredo B P D, Ahmed N, Kim K H, Zuo J-M, Fang N, Ferreira P and Li X 2010 *Nano Lett.* **10** 1582
[107] Ghosh R, Pal A and Giri P K 2015 *J. Raman Spectrosc.* **46** 624
[108] Ghosh R and Giri P K 2016 *Sci. Adv. Today* **2** 25230
[109] Ghosh R, Imakita K, Fujii M and Giri P K 2016 *Phys. Chem. Chem. Phys.* **18** 7715
[110] Savin H, Repo P, von Gastrow G, Ortega P, Calle E, Garín M and Alcubilla R 2015 *Nat. Nanotechnol.* **10** 624
[111] Lin X X, Zeng Y, Zhong S H, Huang Z G, Qian H Q, Ling J, Zhu J B and Shen W Z 2015 *Nanotechnology* **26** 125401
[112] Katiyar A K, Mukherjee S, Zeeshan M, Ray S K and Raychaudhuri A K 2015 *ACS Appl. Mater. Interfaces* **7** 23445
[113] Mankin M N, Day R W, Gao R, No Y-S, Kim S-K, McClelland A A, Bell D C, Park H-G and Lieber C M 2015 *Nano Lett.* **15** 4776
[114] Zhou X T, Zhang R Q, Peng H Y, Shang N G, Wang N, Bello I, Lee C S and Lee S T 2000 *Chem. Phys. Lett.* **332** 215
[115] Liu Y, Vishniakou S, Yoo J and Dayeh S A 2015 *Sci. Rep.* **5** 18482

[116] Zhang X, Xie C, Jie J, Zhang X, Wu Y and Zhang W 2013 *J. Mater. Chem.* A **1** 6593
[117] Lin Y *et al* 2013 *Energy Environ. Sci.* **6** 108
[118] Xie C *et al* 2011 *Appl. Phys. Lett.* **99** 133113
[119] Cho Y J, Kim H S, Im H, Myung Y, Jung G B, Lee C W, Park J, Park M-H, Cho J and Kang H S 2011 *J. Phys. Chem.* C **115** 9451
[120] Wang B, Li X, Zhang X, Luo B, Jin M, Liang M, Dayeh S A, Picraux S T and Zhi L 2013 *ACS Nano* **7** 1437
[121] Lo Faro M J *et al* 2015 *Sci. Rep.* **5** 16753
[122] Kargar A *et al* 2015 *Adv. Funct. Mater.* **25** 2609
[123] Wang W-C, Tsai M-C, Yang J, Hsu C and Chen M-J 2015 *ACS Appl. Mater. Interfaces* **7** 10228
[124] Pan A L, Yao L, Qin Y, Yang Y, Kim D S, Yu R, Zou B, Werner P, Zacharias M and Gösele U 2008 *Nano Lett.* **8** 3413
[125] Yu Y *et al* 2016 *ACS Appl. Mater. Interfaces* **8** 3992
[126] Nguyen H T, Zamfir M R, Duong L D, Lee Y H, Bondavalli P and Pribat D 2012 *J. Mater. Chem.* **22** 24618
[127] Flynn G, Ramasse Q M and Ryan K M 2016 *Nano Lett.* **16** 374
[128] Zhan J, Bando Y, Hu J, Liu Z, Yin L and Golberg D 2005 *Angew. Chem. Int. Ed.* **44** 2140
[129] Wu Y-T, Huang C-W, Chiu C-H, Chang C-F, Chen J-Y, Lin T-Y, Huang Y-T, Lu K-C, Yeh P-H and Wu W-W 2016 *Nano Lett.* **16** 1086
[130] Feng Z, Jia R, Dou B, Li H, Jin Z, Liu X, Li F, Zhang W and Wu C 2015 *Appl. Phys. Lett.* **106** 053118
[131] Huang Y, Ferhan A R, Cho S-J, Lee H and Kim D-H 2015 *ACS Appl. Mater. Interfaces* **7** 17582
[132] Zhao L, Liao K, Pynenburg M, Wong L, Heinig N, Thomas J P and Leung K T 2013 *ACS Appl. Mater. Interfaces* **5** 2410
[133] Chen Y-H, Li W-S, Liu C-Y, Wang C-Y, Chang Y-C and Chen L-J 2013 *J. Mater. Chem.* C **1** 1345
[134] Megouda N, Cofininier Y, Szunerits S, Hadjersi T, ElKechai O and Boukherroub R 2011 *Chem. Commun.* **47** 991
[135] Wang X, Peng K-Q, Pan X-J, Chen X, Yang Y, Li L, Meng X-M, Zhang W-J and Lee S-T 2011 *Angew. Chem. Int. Ed.* **50** 9861
[136] Duan C, Wang H, Zhang B, Li F, Ou X and Zhang X 2015 *Chem. Commun.* **51** 3383
[137] Liu D, Li L, Gao Y, Wang C, Jiang J and Xiong Y 2015 *Angew. Chem. Int. Ed.* **54** 2980
[138] Yuan G D *et al* 2010 *ACS Nano* **4** 3045
[139] Chen Y, Wang X, Erramilli S, Mohanty P and Kalinowski A 2006 *Appl. Phys. Lett.* **89** 223512
[140] Liu N, Yao Y, Cha J J, McDowell M T, Han Y and Cui Y 2011 *Nano Res.* **5** 109
[141] Wang B and Haick H 2013 *ACS Appl. Mater. Interfaces* **5** 2289
[142] Mu L, Chang Y, Sawtelle S D, Wipf M, Duan X and Reed M A 2015 *IEEE Access* **3** 287
[143] Halpern J M, Wang B and Haick H 2015 *ACS Appl. Mater. Interfaces* **7** 11315
[144] Kim D R, Lee C H and Zheng X 2010 *Nano Lett.* **10** 1050
[145] Demichel O, Calvo V, Besson A, Noe P, Salem B, Pauc N, Oehler F, Gentile P and Magnea N 2010 *Nano Lett.* **10** 2323
[146] Walavalkar S S, Hofmann C E, Homyk A P, Henry M D, Atwater H A and Scherer A 2010 *Nano Lett.* **10** 4423
[147] Valenta J, Bruhn B and Linnros J 2011 *Nano Lett.* **11** 3003
[148] Skuja L, Suzuki T and Tanimura K 1995 *Phys. Rev.* B **52** 15208
[149] Chan Y F, Su W, Zhang C X, Wu Z L, Tang Y, Sun X Q and Xu H J 2012 *Opt. Express* **20** 24280
[150] Tan S T, Sun X W, Zhao J L, Iwan S, Cen Z H, Chen T P, Ye J D, Lo G Q, Kwong D L and Teo K L 2008 *Appl. Phys. Lett.* **93** 013506
[151] Yuan-Ming C, Sheng-Rui J, Hsin-Yi L, Chih-Ming L and Jenh-Yih J 2010 *Nanotechnology* **21** 385705
[152] Moon K-J, Lee T I, Lee W and Myoung J-M 2014 *Nanoscale* **6** 3611
[153] Hsieh Y-P *et al* 2009 *Nano Lett.* **9** 1839
[154] Kang Z, Liu Y and Lee S-T 2011 *Nanoscale* **3** 777
[155] Osminkina L A, Sivakov V A, Mysov G A, Georgobiani V A, Natashina U A, Talkenberg F, Solovyev V V, Kudryavtsev A A and Timoshenko V Y 2014 *Nanoscale Res. Lett.* **9** 1
[156] Bassu M, Strambini M L, Barillaro G and Fuso F 2010 *Appl. Phys. Lett.* **97** 143113
[157] Yuan G, Aruda K, Zhou S, Levine A, Xie J and Wang D 2011 *Angew. Chem. Int. Ed.* **50** 2334
[158] Peng K, Xu Y, Wu Y, Yan Y, Lee S-T and Zhu J 2005 *Small* **1** 1062
[159] Togonal A S, Foldyna M, Chen W, Wang J X, Neplokh V, Tchernycheva M, Nassar J, Roca i Cabarrocas P and Rusli 2016 *J. Phys. Chem.* C **120** 2962
[160] Petterson M K, Lemaitre M G, Shen Y, Wadhwa P, Hou J, Vasilyeva S V, Kravchenko I I and Rinzler A G 2015 *ACS Appl. Mater. Interfaces* **7** 21182
[161] Lai Y-C *et al* 2016 *Opt. Express* **24** A414
[162] Kim D R, Lee C H, Rao P M, Cho I S and Zheng X 2011 *Nano Lett.* **11** 2704
[163] Ko M-D, Rim T, Kim K, Meyyappan M and Baek C-K 2015 *Sci. Rep.* **5** 11646
[164] Wang W, Zhao Q, Laurent K, Leprince-Wang Y, Liao Z-M and Yu D 2012 *Nanoscale* **4** 261
[165] Shen X, Sun B, Liu D and Lee S-T 2011 *J. Am. Chem. Soc.* **133** 19408
[166] Peng K, Wang X and Lee S-T 2008 *Appl. Phys. Lett.* **92** 163103
[167] Kim J, Jung C-L, Kim M, Kim S, Kang Y, Lee H-S, Park J, Jun Y and Kim D 2016 *Nanoscale* **8** 7761
[168] Hochbaum A I, Chen R, Delgado R D, Liang W, Garnett E C, Najarian M, Majumdar A and Yang P 2008 *Nature* **451** 163
[169] Li C, Krali E, Fobelets K, Cheng B and Wang Q 2012 *Appl. Phys. Lett.* **101** 222101
[170] Lee E K *et al* 2012 *Nano Lett.* **12** 2918
[171] Yang K, Cantarero A, Rubio A and D'Agosta R 2015 *Nano Res.* **8** 2611
[172] Zhang L, Liu C, Wong A B, Resasco J and Yang P 2015 *Nano Res.* **8** 281
[173] Liu Q, Wu F, Cao F, Chen L, Xie X, Wang W, Tian W and Li L 2015 *Nano Res.* **8** 1
[174] Boettcher S W *et al* 2011 *J. Am. Chem. Soc.* **133** 1216
[175] Liu C, Dasgupta N P and Yang P 2014 *Chem. Mater.* **26** 415
[176] LaTempa T J, Rani S, Bao N and Grimes C A 2012 *Nanoscale* **4** 2245
[177] Torralba-Peñalver E, Luo Y, Compain J-D, Chardon-Noblat S and Fabre B 2015 *ACS Catal.* **5** 6138
[178] Liu R, Yuan G, Joe C L, Lightburn T E, Tan K L and Wang D 2012 *Angew. Chem. Int. Ed.* **51** 6709
[179] Cui L-F, Ruffo R, Chan C K, Peng H and Cui Y 2009 *Nano Lett.* **9** 491
[180] Bogart T D, Oka D, Lu X, Gu M, Wang C and Korgel B A 2014 *ACS Nano* **8** 915
[181] Wang B, Li X, Luo B, Jia Y and Zhi L 2013 *Nanoscale* **5** 1470
[182] Xia F, Kwon S, Lee W W, Liu Z, Kim S, Song T, Choi K J, Paik U and Park W I 2015 *Nano Lett.* **15** 6658
[183] Chan C K, Patel R N, O'Connell M J, Korgel B A and Cui Y 2010 *ACS Nano* **4** 1443
[184] Chen H, Xiao Y, Wang L and Yang Y 2011 *J. Power Sources* **196** 6657
[185] Kohandehghan A, Cui K, Kupsta M, Memarzadeh E, Kalisvaart P and Mitlin D 2014 *J. Mater. Chem.* A **2** 11261

[186] Memarzadeh E L, Kalisvaart W P, Kohandehghan A, Zahiri B, Holt C M B and Mitlin D 2012 *J. Mater. Chem.* **22** 6655
[187] Kohandehghan A, Kalisvaart P, Kupsta M, Zahiri B, Amirkhiz B S, Li Z, Memarzadeh E L, Bendersky L A and Mitlin D 2013 *J. Mater. Chem.* A **1** 1600
[188] Chockla A M, Bogart T D, Hessel C M, Klavetter K C, Mullins C B and Korgel B A 2012 *J. Phys. Chem.* C **116** 18079
[189] Memarzadeh Lotfabad E, Kalisvaart P, Cui K, Kohandehghan A, Kupsta M, Olsen B and Mitlin D 2013 *Phys. Chem. Chem. Phys.* **15** 13646
[190] Kohandehghan A, Kalisvaart P, Cui K, Kupsta M, Memarzadeh E and Mitlin D 2013 *J. Mater. Chem.* A **1** 12850
[191] Yao Y, Liu N, McDowell M T, Pasta M and Cui Y 2012 *Energy Environ. Sci.* **5** 7927
[192] McSweeney W, Geaney H and O'Dwyer C 2015 *Nano Res.* **8** 1395
[193] Wang J, Meng X, Fan X, Zhang W, Zhang H and Wang C 2015 *ACS Nano* **9** 6576
[194] Wang X-L and Han W-Q 2010 *ACS Appl. Mater. Int.* **2** 3709
[195] Liang B, Liu Y and Xu Y 2014 *J. Power Sources* **267** 469
[196] Kennedy T, Brandon M and Ryan K M 2016 *Adv. Mater.* **28** 5696
[197] Chang S-W, Oh J, Boles S T and Thompson C V 2010 *Appl. Phys. Lett.* **96** 153108
[198] Lu F, Qiu M, Qi X, Yang L, Yin J, Hao G, Feng X, Li J and Zhong J 2011 *Appl. Phys.* A **104** 545
[199] Alper J P, Vincent M, Carraro C and Maboudian R 2012 *Appl. Phys. Lett.* **100** 163901
[200] Dubal D P, Aradilla D, Bidan G, Gentile P, Schubert T J S, Wimberg J, Sadki S and Gomez-Romero P 2015 *Sci. Rep.* **5** 9771
[201] Han H-C *et al* 2013 *Nano Lett.* **13** 1422
[202] Devarapalli R R, Szunerits S, Coffinier Y, Shelke M V and Boukherroub R 2016 *ACS Appl. Mater. Interfaces* **8** 4298
[203] Aradilla D, Bidan G, Gentile P, Weathers P, Thissandier F, Ruiz V, Gomez-Romero P, Schubert T J S, Sahin H and Sadki S 2014 *RSC Adv.* **4** 26462
[204] Aradilla D *et al* 2016 *ACS Appl. Mater. Int.* **8** 18069
[205] Aradilla D *et al* 2015 *J. Mater. Chem.* A **3** 13978
[206] Liao F, Wang T and Shao M 2015 *J. Mater. Sci. Mater. Electron.* **26** 4722
[207] Song H S *et al* 2011 *Cryst. Growth Des.* **11** 147
[208] Chia-Yun C and Arh-Hwang C 2012 *J. Phys. D: Appl. Phys.* **45** 365304
[209] Wang H, Jiang W, Yuan L, Wang L and Chen H 2013 *ACS Appl. Mater. Interfaces* **5** 1800
[210] Wang H, Jiang W, Wang Y, Liu X, Yao J, Yuan L, Wu Z, Li D, Song B and Chen H 2013 *Langmuir* **29** 3
[211] Cui Y, Wei Q, Park H and Lieber C 2001 *Science* **293** 1289
[212] Luo L, Jie J, Zhang W, He Z, Wang J, Yuan G, Zhang W, Wu L C M and Lee S-T 2009 *Appl. Phys. Lett.* **94** 193101
[213] Wipf M, Stoop R L, Tarasov A, Bedner K, Fu W, Wright I A, Martin C J, Constable E C, Calame M and Schönenberger C 2013 *ACS Nano* **7** 5978
[214] Zhang C X, Liu L, Yin H J, Fang H, Zhao Y M, Bi C J and Xu H J 2014 *Appl. Phys. Lett.* **105** 011905
[215] Han X, Wang H, Ou X and Zhang X 2012 *J. Mater. Chem.* **22** 14127
[216] Yang X, Zhong H, Zhu Y, Shen J and Li C 2013 *Dalton Trans.* **42** 14324
[217] Zhang B, Wang H, Lu L, Ai K, Zhang G and Cheng X 2008 *Adv. Funct. Mater.* **18** 2348
[218] Huang J-A, Zhao Y-Q, Zhang X-J, He L-F, Wong T-L, Chui Y-S, Zhang W-J and Lee S-T 2013 *Nano Lett.* **13** 5039
[219] Zhuo S, Shao M, Cheng L, Que R, Zhuo S, Duo Ma D D and Lee S-T 2010 *Appl. Phys. Lett.* **96** 103108
[220] Wang H, Mu L, She G and Shi W 2015 *RSC Adv.* **5** 65905
[221] Chen K-I, Li B-R and Chen Y-T 2011 *Nano Today* **6** 131
[222] Zhang G-J and Ning Y 2012 *Anal. Chim. Acta* **749** 1
[223] Rim T, Baek C-K, Kim K, Jeong Y-H, Lee J-S and Meyyappan M 2014 *J. Nanosci. Nanotechnol.* **14** 273
[224] Chen H-C, Chen Y-T, Tsai R-Y, Chen M-C, Chen S-L, Xiao M-C, Chen C-L and Hua M-Y 2015 *Biosens. Bioelectron.* **66** 198
[225] Nuzaihan M N M, Hashim U, Md Arshad M K, Kasjoo S R, Rahman S F A, Ruslinda A R, Fathil M F M, Adzhri R and Shahimin M M 2016 *Biosens. Bioelectron.* **83** 106
[226] Adam T and Hashim U 2015 *Biosens. Bioelectron.* **67** 656
[227] Kihyun K, Taiuk R, Chanoh P, Donghoon K, Meyyappan M and Jeong-Soo L 2014 *Nanotechnology* **25** 345501
[228] Xu T-T, Huang J-A, He L-F, He Y, Su S and Lee S-T 2011 *Appl. Phys. Lett.* **99** 153116
[229] Zhang M-L, Yi C-Q, Fan X, Peng K-Q, Wong N-B, Yang M-S, Zhang R-Q and Lee S-T 2008 *Appl. Phys. Lett.* **92** 043116
[230] Akin M S, Yilmaz M, Babur E, Ozdemir B, Erdogan H, Tamer U and Demirel G 2014 *J. Mater. Chem.* B **2** 4894
[231] Su S, Wei X, Zhong Y, Guo Y, Su Y, Huang Q, Lee S-T, Fan C and He Y 2012 *ACS Nano* **6** 2582
[232] Han S W, Lee S, Hong J, Jang E, Lee T and Koh W-G 2013 *Biosens. Bioelectron.* **45** 129
[233] Han J-W, Rim T, Baek C-K and Meyyappan M 2015 *ACS Appl. Mater. Interfaces* **7** 21263
[234] Noh J-S, Kim H, Kim B S, Lee E, Cho H H and Lee W 2011 *J. Mate. Chem.* **21** 15935
[235] McAlpine M C, Agnew H D, Rohde R D, Blanco M, Ahmad H, Stuparu A D, Goddard W A and Heath J R 2008 *J. Am. Chem. Soc.* **130** 9583
[236] Liao J, Li Z, Wang G, Chen C, Lv S and Li M 2016 *Phys. Chem. Chem. Phys.* **18** 4835
[237] Chen X, Zhang J, Wang Z, Yan Q and Hui S 2011 *Sensors Actuators* B **156** 631
[238] Engel Y, Elnathan R, Pevzner A, Davidi G, Flaxer E and Patolsky F 2010 *Angew. Chem. Int. Ed.* **49** 6830
[239] Shehada N, Brönstrup G, Funka K, Christiansen S, Leja M and Haick H 2015 *Nano Lett.* **15** 1288
[240] Ma S, Hu M, Zeng P, Li M, Yan W and Qin Y 2014 *Sensors Actuators* B **192** 341